AXONAL DEGENERATION

RIPK1 mediates axonal degeneration by promoting inflammation and necroptosis in ALS

Yasushi Ito,[1] Dimitry Ofengeim,[1] Ayaz Najafov,[1] Sudeshna Das,[2] Shahram Saberi,[3,4] Ying Li,[1,5] Junichi Hitomi,[1] Hong Zhu,[1] Hongbo Chen,[1] Lior Mayo,[6] Jiefei Geng,[1] Palak Amin,[1] Judy Park DeWitt,[1] Adnan Kasim Mookhtiar,[1] Marcus Florez,[1] Amanda Tomie Ouchida,[1] Jian-bing Fan,[7] Manolis Pasparakis,[8] Michelle A. Kelliher,[9] John Ravits,[3,4] Junying Yuan[1,5]*

Mutations in the *optineurin* (*OPTN*) gene have been implicated in both familial and sporadic amyotrophic lateral sclerosis (ALS). However, the role of this protein in the central nervous system (CNS) and how it may contribute to ALS pathology are unclear. Here, we found that optineurin actively suppressed receptor-interacting kinase 1 (RIPK1)–dependent signaling by regulating its turnover. Loss of OPTN led to progressive dysmyelination and axonal degeneration through engagement of necroptotic machinery in the CNS, including RIPK1, RIPK3, and mixed lineage kinase domain–like protein (MLKL). Furthermore, RIPK1- and RIPK3-mediated axonal pathology was commonly observed in *SOD1*^{G93A} transgenic mice and pathological samples from human ALS patients. Thus, RIPK1 and RIPK3 play a critical role in mediating progressive axonal degeneration. Furthermore, inhibiting RIPK1 kinase may provide an axonal protective strategy for the treatment of ALS and other human degenerative diseases characterized by axonal degeneration.

Loss-of-function mutations in the *optineurin* (*OPTN*) gene have been implicated in both familial and sporadic cases of amyotrophic lateral sclerosis (ALS), a devastating degenerative motor neuron disease (*1*–*3*). The *Optn* gene encodes a ubiquitin-binding protein involved in tumor necrosis factor–α (TNFα) signaling but is dispensable for nuclear factor κB (NF-κB) activation (*4*, *5*). It is still unclear how the loss of function of *OPTN* leads to human ALS.

Receptor-interacting kinase 1 (RIPK1) is a critical regulator of cell death and inflammation (*6*). RIPK1 regulates necroptosis, a form of regulated necrotic cell death, by promoting the sequential activation of two downstream targets, RIPK3 and mixed lineage kinase domain–like protein (MLKL) (*7*–*9*). Application of necrostatin-1 (7-Cl-O-Nec-1) (Nec-1s), a highly specific inhibitor of RIPK1 kinase activity, blocks necroptosis and inflammation in vitro and in vivo (*10*, *11*). However, the pathophysiological significance of RIPK1 and necroptosis in the genetic context of human diseases remains to be established.

ALS belongs to axonal "dying back" neurodegenerative diseases, as the onset begins with axonal pathology. Axonal degeneration makes a substantial contribution to neurological disability in these patients (*12*). Axonal degeneration induced by direct nerve injury—known as Wallerian degeneration—is mediated through a mechanism distinct from apoptosis of neuronal cell bodies (*13*, *14*). Axonal degeneration in patients with neurodegenerative diseases such as ALS may also exhibit features similar to those of Wallerian degeneration and is referred to as "Wallerian-like" degeneration. The mechanism of Wallerian or Wallerian-like degeneration is still unclear.

To understand the mechanism by which the loss of OPTN could lead to ALS, we developed *Optn*$^{-/-}$ mice (fig. S1, A and B). We examined the impact of *Optn* loss in the spinal cord of *Optn*$^{-/-}$ mice. The number and morphology of spinal cord motor neurons in *Optn*$^{-/-}$ mice were indistinguishable from wild-type (WT) mice (fig. S1, C and D). However, from the age of 3 weeks to 2 years, we observed a marked reduction in the number of motor axons and abnormal myelination in the ventrolateral spinal cord white matter in the *Optn*$^{-/-}$ mice (Fig. 1, A to D, and fig. S1E). The axonal pathology presented as a decompaction of myelin sheaths with a decreased g-ratio (axon diameter/axon-plus-myelin diameter), an increased number of large-diameter axons, and a decreased axonal number in the ventrolateral white matter (Fig. 1, B to D), which suggested degeneration and swelling of motor neuron axons in *Optn*$^{-/-}$ mice. This finding is similar to the axonal pathology observed in the spinal cords of ALS patients in the early stages of the disease (*15*). The pathology was progressive—a reduction in axonal numbers was observed at 12 weeks or older but not at 3 weeks (fig. S1F). Similar pathology was observed in the ventral roots of motor axons in *Optn*$^{-/-}$ mice (fig. S1, G to J). In addition, denervation of neuromuscular junctions in the tibialis anterior muscle was observed in *Optn*$^{-/-}$ mice (fig. S1, K and L). Thus, OPTN deficiency leads to axonal pathology without affecting motor neuron cell bodies. Consistent with this notion, we observed a significant increase in the number of cells positive for terminal deoxynucleotidyl transferase–mediated deoxyuridine triphosphate nick end labeling (TUNEL^{+} cells) in the ventrolateral white matter of spinal cords of *Optn*$^{-/-}$ mice (Fig. 1E). Thus, Optn deficiency sensitizes cells to cell death in the spinal cord white matter of *Optn*$^{-/-}$ mice.

To determine the cell types involved in mediating Optn deficiency–induced axonal degeneration, we generated lineage-specific deletion of Optn using *Cnp-cre*, *Lyz2-cre*, *Gfap-cre*, and *Mnx1-cre* mice (*16*–*18*) (fig. S2). Loss of Optn from oligodendrocytes and myeloid cells, but not from astrocytes or motor neurons, was sufficient to reproduce axonal myelination pathology (Fig. 1, F to I). Furthermore, we induced Optn loss from the microglial lineage by dosing *Optn*$^{F/F}$;*Cx3cr1*^{Cre} mice (*19*) with tamoxifen for 1 month (fig. S3A) and also found axonal pathology like that in *Optn*$^{-/-}$ mice (fig. S3, B to E).

We found that knockdown of Optn sensitized cells to necroptosis in our genome-wide small interfering RNA screen (*20*, *21*) (Z-score = –2.07) (table S1). We further confirmed that knockdown of *Optn* sensitized L929 cells to necroptosis induced by TNFα or zVAD.fmk (fig. S4, A and B). zVAD-induced necrosis is known to involve autocrine TNFα activity (*22*). Thus, *Optn* deficiency sensitized cells to necroptosis (fig. S4C). The biochemical hallmarks of necroptosis—including the upshifts of Ripk1, Ripk3, and phospho-MLKL (p-MLKL), as well as the levels of complex IIb—were significantly higher in *Optn*$^{-/-}$ mouse embryo fibroblasts (MEFs) than in *Optn*$^{+/+}$ MEFs stimulated by TNFα, zVAD, or cycloheximide (fig. S4D). Note that *Optn*$^{-/-}$ oligodendrocytes were sensitized to die by TNFα-induced necroptosis but were protected by Nec-1s and in *Optn*$^{-/-}$;*Ripk1*$^{D138N/D138N}$ and *Optn*$^{-/-}$;*Ripk3*$^{-/-}$ double mutants (*23*, *24*) (Fig. 2A). Thus, Optn deficiency can promote necroptosis of oligodendrocytes.

The expression levels of Ripk1, Ripk3, and MLKL—the key mediators of necroptosis—were all increased in the spinal cords of *Optn*$^{-/-}$ mice (Fig. 2B). Furthermore, we detected the interaction of Optn and Ripk1 in spinal cords from WT mice (Fig. 2C). Compared with WT mice, RIPK1 lysine 48 (K48) ubiquitination levels were decreased, whereas Ripk1 mRNA was unchanged in the spinal cords of *Optn*$^{-/-}$ mice (Fig. 2, D and E). Furthermore, Ripk1 was degraded more slowly in *Optn*$^{-/-}$ MEFs than that in WT cells

[1]Department of Cell Biology, Harvard Medical School, 240 Longwood Avenue, Boston, MA 02115, USA. [2]MassGeneral Institute for Neurodegenerative Disease, Massachusetts General Hospital, Cambridge, MA 02139, USA. [3]Department of Neurology, Harvard Medical School, Boston, MA 02115, USA. [4]ALS Translational Research Program, Department of Neurosciences, University of California, San Diego, La Jolla, CA 92093, USA. [5]Interdisciplinary Research Center on Biology and Chemistry, Shanghai Institute of Organic Chemistry, Chinese Academy of Sciences, 26 QiuYue Road, PuDong District, Shanghai, 201210, China. [6]Ann Romney Center for Neurologic Diseases, Brigham and Women's Hospital, Harvard Medical School, Boston, MA 02115, USA. [7]Illumina, Inc., San Diego, CA 92122, USA. [8]Institute for Genetics, University of Cologne, 50674 Cologne, Germany. [9]Department of Cancer Biology, University of Massachusetts Medical School, Worcester, MA 01605, USA.
*Corresponding author. Email: jyuan@hms.harvard.edu

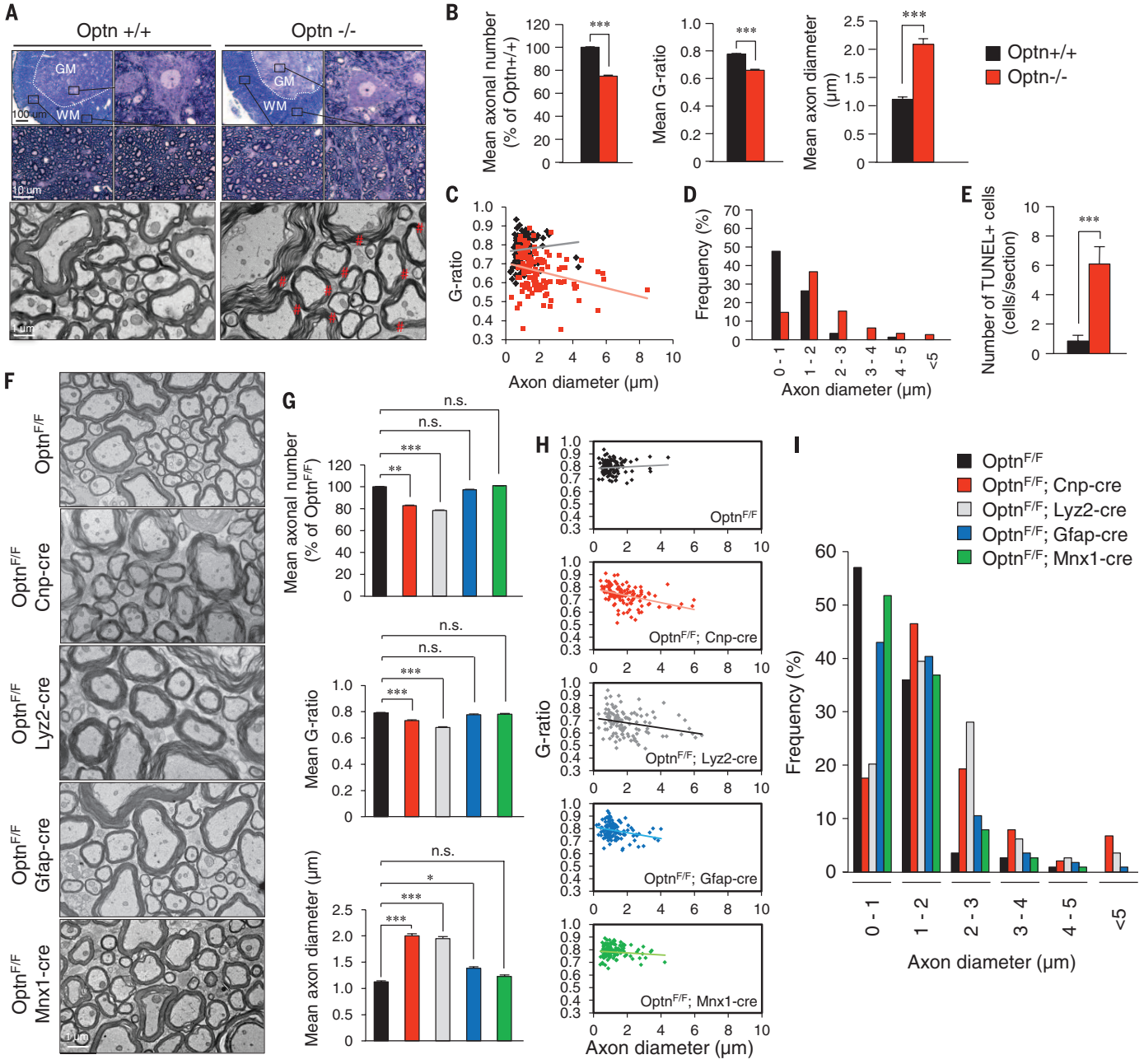

Fig. 1. Optn deficiency in oligodendrocyte and myeloid lineages promotes axonal loss and dysmyelination in the spinal cords of *Optn*$^{-/-}$ mice. (**A**) (Top) Toluidine blue–stained sections from the ventrolateral lumbar spinal cords of WT and *Optn*$^{-/-}$ mice. The boxes show axons in the ventrolateral lumbar spinal cord white matter and the motor neurons in the ventral lumbar spinal cord gray matter, respectively. (Bottom) Electron microscopic analysis of motor axonal myelination in the ventrolateral lumbar spinal cords from WT and *Optn*$^{-/-}$ mice. (**B** to **D** and **F** to **I**) The mean axonal numbers, mean g-ratios, and mean axonal diameters; individual g-ratio distribution; and distributions of axonal diameters in the ventrolateral lumbar spinal cord white matter (L1 to L4) of WT, *Optn*$^{-/-}$ mice, *Optn*$^{F/F}$ mice, *Optn*$^{F/F}$;*Cnp-cre* mice, *Optn*$^{F/F}$;*Lyz2-cre* mice, *Optn*$^{F/F}$;*Gfap-cre* mice, and *Optn*$^{F/F}$;*Mnx1-cre* mice, as indicated. (**E**) The number of TUNEL^{+} cells in the lumbar spinal cords (L1 to L4, one section each) of indicated genotype (five mice for each genotype).

(Fig. 2F). Thus, OPTN might control sensitivity to necroptosis by regulating proteasomal turnover of RIPK1.

Phospho-Ser$^{14/15}$, a marker of Ripk1 activation, was increased in *Optn*$^{-/-}$ microglia relative to WT microglia, which were inhibited by Nec-1s and *Ripk1*$^{D138N/D138N}$ mutation (Fig. 2G). Because microglia express little MLKL, we hypothesize that Ripk1 activation in microglia promotes inflammatory signaling not necroptosis. Consistent with this notion, we detected an increased production of multiple proinflammatory cytokines—including interleukins IL-1α, IL-1β, IL-2, and IL-12; interferon-γ (IFN-γ); and TNFα in the spinal cords of *Optn*$^{-/-}$ mice—which were markedly reduced in the *Optn*$^{-/-}$;*Ripk1*$^{D138N/D138N}$ mice (Fig. 2H). In addition, *Optn*$^{-/-}$ microglia had elevated TNFα, which was inhibited by Nec-1s (fig. S5A). As predicted, the levels of TNFα were also increased in the spinal cords of *Optn*$^{F/F}$;*Lyz2-cre* mice (fig. S5B).

To explore the effect of Optn deficiency on transcriptions, we performed RNA sequencing on WT, *Optn*$^{-/-}$, and *Optn*$^{-/-}$;*Ripk1*$^{D138N/D138N}$ primary microglia. Coexpression analysis (*25*) identified a module with ~1300 genes (ME1) differentially expressed between WT and *Optn*$^{-/-}$ microglia and suppressed by *Ripk1*$^{D138N/D138N}$.

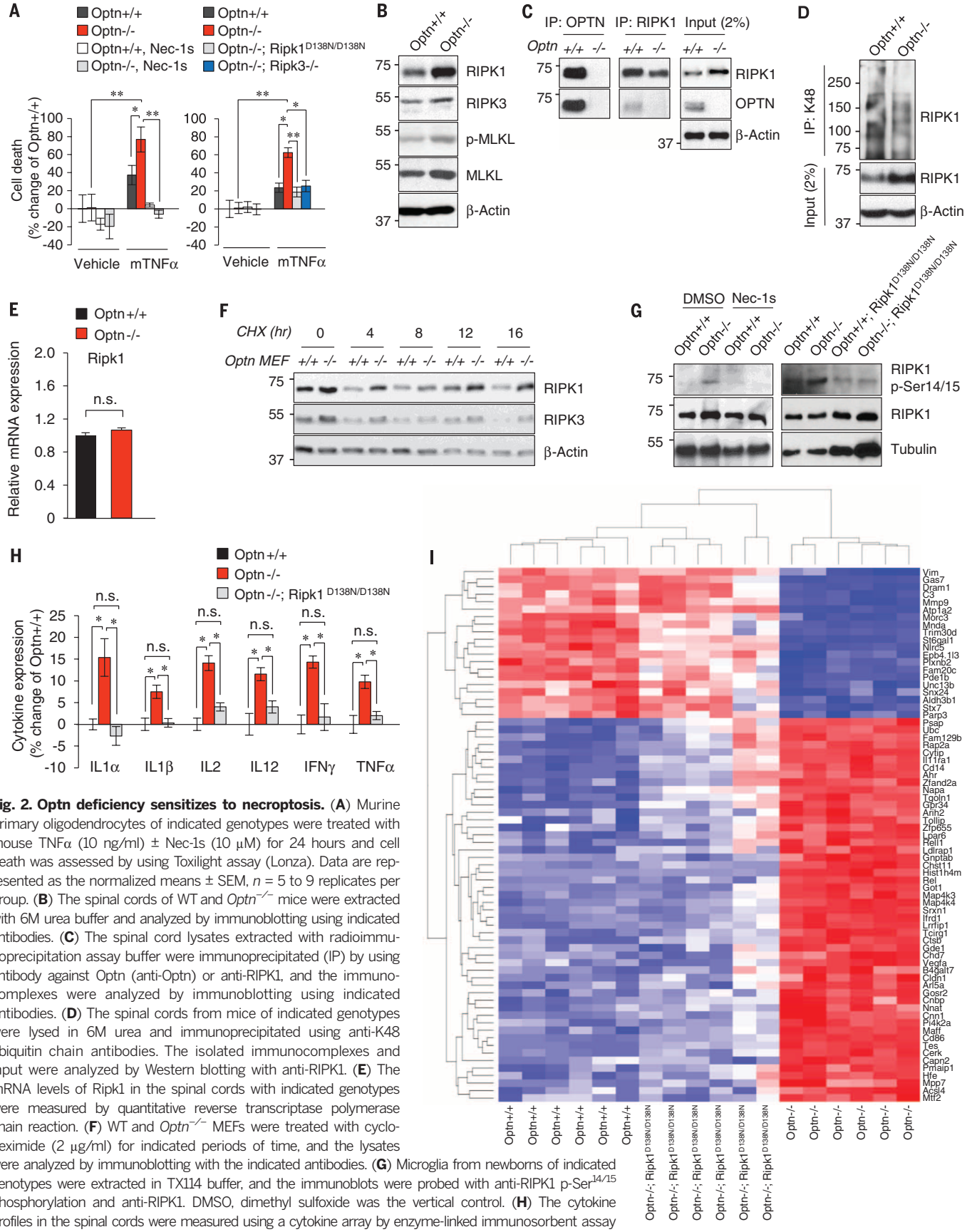

Fig. 2. Optn deficiency sensitizes to necroptosis. (**A**) Murine primary oligodendrocytes of indicated genotypes were treated with mouse TNFα (10 ng/ml) ± Nec-1s (10 μM) for 24 hours and cell death was assessed by using Toxilight assay (Lonza). Data are represented as the normalized means ± SEM, $n = 5$ to 9 replicates per group. (**B**) The spinal cords of WT and *Optn*$^{-/-}$ mice were extracted with 6M urea buffer and analyzed by immunoblotting using indicated antibodies. (**C**) The spinal cord lysates extracted with radioimmunoprecipitation assay buffer were immunoprecipitated (IP) by using antibody against Optn (anti-Optn) or anti-RIPK1, and the immunocomplexes were analyzed by immunoblotting using indicated antibodies. (**D**) The spinal cords from mice of indicated genotypes were lysed in 6M urea and immunoprecipitated using anti-K48 ubiquitin chain antibodies. The isolated immunocomplexes and input were analyzed by Western blotting with anti-RIPK1. (**E**) The mRNA levels of Ripk1 in the spinal cords with indicated genotypes were measured by quantitative reverse transcriptase polymerase chain reaction. (**F**) WT and *Optn*$^{-/-}$ MEFs were treated with cycloheximide (2 μg/ml) for indicated periods of time, and the lysates were analyzed by immunoblotting with the indicated antibodies. (**G**) Microglia from newborns of indicated genotypes were extracted in TX114 buffer, and the immunoblots were probed with anti-RIPK1 p-Ser$^{14/15}$ phosphorylation and anti-RIPK1. DMSO, dimethyl sulfoxide was the vertical control. (**H**) The cytokine profiles in the spinal cords were measured using a cytokine array by enzyme-linked immunosorbent assay (ELISA). (**I**) Heat map of the top 71 genes in the module ME1 differentially expressed in microglia of indicated genotypes. Low expression is shown in blue and high expression, in red.

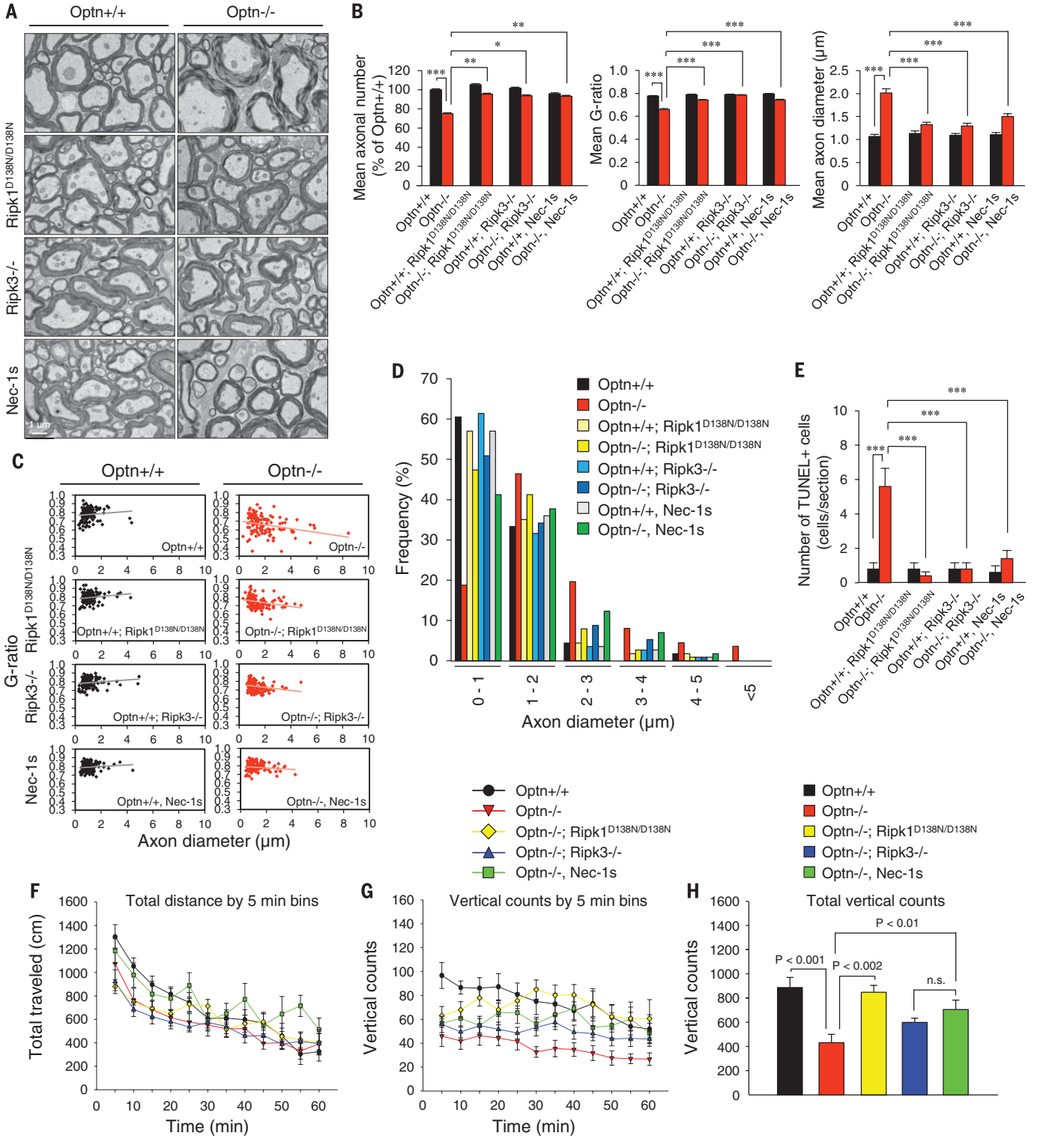

Fig. 3. Ripk1 and Ripk3 mediate axonal pathology in the spinal cords of *Optn*$^{-/-}$ mice. (**A**) Dysmyelination in the spinal cords of *Optn*$^{-/-}$ mice was blocked by genetically inhibiting Ripk1 in *Optn*$^{-/-}$;*Ripk1*$^{D138N/D138N}$ mice, pharmacologically inhibiting Ripk1 by Nec-1s (oral dosing of Nec-1s for 1 month starting from 8 weeks of age), and by loss of Ripk3 in *Optn*$^{-/-}$;*Ripk3*$^{-/-}$ mice. (**B** to **D**) Mean axonal numbers, g-ratios, and axonal diameters (B); individual g-ratio distributions (C); and axonal diameter distributions (D). (**E**) The number of TUNEL^{+} cells in the lumbar spinal cords (L1 to L4, one section each) of indicated genotypes at 3 months of age (five mice per genotype). (**F** to **H**) Mice of indicated genotypes were tested in open-field test for spontaneous motor activity. The mice were at 3 months of age and 28 to 32 g of body weight (no statistically significant difference in body weight between different groups). The total distance traveled in 1 hour showed no difference between different groups (F). *Optn*$^{-/-}$ mice showed a significant deficit on the vertical rearing activity (frequency with which the mice stood on their hind legs). This deficit was blocked after dosing with Nec-1s for 1 month starting from 8 weeks old and in *Optn*$^{-/-}$;*Ripk1*$^{D138N/D138N}$ double-mutant mice and reduced in *Optn*$^{-/-}$;*Ripk3*$^{-/-}$ double-mutant mice (G and H).

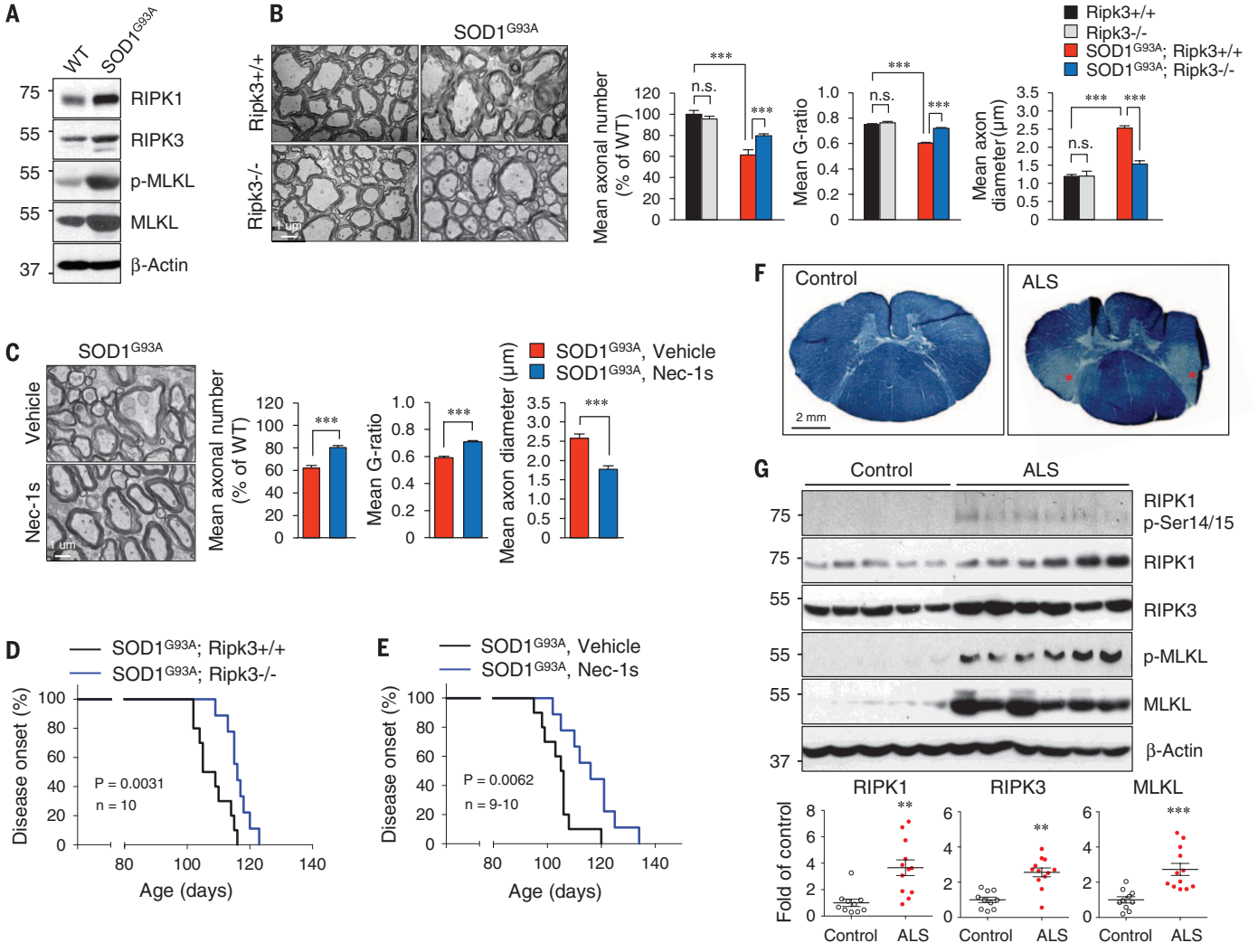

Fig. 4. RIPK1- and RIPK3-mediated axonal pathology is a common mechanism in ALS. (**A**) Urea buffer lysates of spinal cords from WT and *SOD1*^{G93A} transgenic mice (12 weeks of age) were analyzed by immunoblotting using indicated antibodies. (**B** and **C**) The myelination morphology (top), mean axonal numbers (bottom), mean g-ratios (bottom), mean axonal diameters (bottom) of the ventrolateral lumbar spinal cord white matter of *SOD1*^{G93A} mice, *SOD1*^{G93A};*Ripk3*$^{-/-}$ mice (12 weeks of age), and *SOD1*^{G93A} mice dosed with vehicle or Nec-1s for 1 month starting from 8 weeks of age. (**D** and **E**) Ripk3 deficiency (D) and inhibition of Ripk1 by Nec-1s starting from 8 weeks of age (E) delayed the onset of motor dysfunction in *SOD1*^{G93A} mice. (**F**) Sections of pathological spinal cords from a human control and an ALS patient were stained with Luxol fast blue for myelin to show reduced myelination in the lateral column of lower spinal cords of ALS patients. (**G**) Immunoblotting analysis of human control and ALS spinal cord samples using indicated antibodies (top) and the quantification of RIPK1, RIPK3, and MLKL levels from 10 controls and 13 ALS patients (bottom).

The top 71 genes in this module include CD14 and CD86, biomarkers for the proinflammatory M1-like state (*26*) (Fig. 2I and table S2). Elevated CD14 and CD86 in *Optn*$^{-/-}$ microglia were suppressed by Nec-1s and *Ripk1*$^{D138N/D138N}$ (fig. S5C). Thus, Optn deficiency promotes an M1-like inflammatory microglia.

We analyzed the genes differentially expressed in *Optn*$^{-/-}$ microglia using MSigDB (Molecular Signatures Database) (*27*) to identify transcription factors with targets that were overrepresented. We found a significant overrepresentation of the predicted Sp1 transcription factor targets in the ME1 module (table S3) with a network (*28*) of 225 Sp1 targets regulated by RIPK1 (fig. S6A). Increased production of TNFα and the death of L929 cells were blocked by knockdown of Sp1 and by Nec-1s (fig. S6, B and C). Thus, loss of Optn in the spinal cord may increase RIPK1-dependent inflammation.

We examined the involvement of necroptosis in *Optn*$^{-/-}$ mice in vivo. The increase in TUNEL^{+} cells and the axonal pathology of *Optn*$^{-/-}$ mice were all rescued in the *Optn*$^{-/-}$;*Ripk1*$^{D138N/D138N}$ double-mutant and the *Optn*$^{-/-}$;*Ripk3*$^{-/-}$ double-mutant mice and by Nec-1s (Fig. 3, A to E). Behaviorally, *Optn*$^{-/-}$ mice showed no difference in total locomotor activity, whereas the vertical rearing activity was significantly reduced compared with that of WT mice (Fig. 3, F to H). Thus, Optn deficiency leads to hindlimb weakness. Furthermore, the vertical rearing deficit in *Optn*$^{-/-}$ mice was rescued pharmacologically by Nec-1s and genetically in the *Optn*$^{-/-}$;*Ripk1*$^{D138N/D138N}$ mice and *Optn*$^{-/-}$;*Ripk3*$^{-/-}$ mice. Thus, Optn deficiency leads to the activation of necroptotic machinery to promote axonal pathology.

To explore the involvement of RIPK1-mediated axonal pathology in ALS in general, we used *SOD1*^{G93A} transgenic mice. Oligodendrocytes in *SOD1*^{G93A} mice degenerate early, but the mechanism is unclear (*29*). We found that the expression of Ripk1, Ripk3, and MLKL in the spinal cords of *SOD1*^{G93A} transgenic mice was elevated (Fig. 4A). In addition, we observed a similar axonal pathology as that of *Optn*$^{-/-}$ mice in *SOD1*^{G93A} mice before the onset of motor dysfunction (Fig. 4, B and C). Furthermore, these axonal myelination defects were blocked and motor dysfunction onset was delayed genetically by *Ripk3* knockout or by oral administration

of Nec-1s (Fig. 4, D and E). Thus, although we cannot rule out the contribution of Ripk1 or other proapoptotic factors to the degeneration of motor neuron cell bodies (*30*, *31*), the activation of necroptosis contributes to axonal pathology and motor dysfunction in the $SOD1^{G93A}$ transgenic mice.

We next characterized the role of RIPK1 and necroptosis in human ALS. We found evidence of demyelination in the lateral column white matter of lower spinal cord pathological samples from ALS patients as reported (Fig. 4F). In human ALS pathological samples, we also detected multiple biochemical hallmarks of necroptosis, including increased levels of RIPK1, RIPK3, and MLKL and increased RIPK1 p-$Ser^{14/15}$ and p-MLKL in both microglia and oligodendrocytes (Fig. 4G, fig. S7, and table S4). Note that p-MLKL was primarily localized in the white matter, where demyelination was found.

Taken together, our results provide a direct connection between Wallerian-like degeneration induced by OPTN deficiency and RIPK1-regulated necroptosis and inflammation. By promoting both inflammation and cell death, RIPK1 may be a common mediator of axonal pathology in ALS (fig. S8). Because RIPK1 is recruited specifically to the TNF receptor TNFR1 to mediate the deleterious effect of TNFα (*32*), blocking RIPK1 may provide a therapeutic option for the treatment of ALS without affecting TNFR2. Finally, given the recruitment of OPTN to intracellular protein aggregates found in pathological samples from patients with Alzheimer's disease, Parkinson's disease, Creutzfeldt-Jakob disease, multiple system atrophy, and Pick's disease (*33*, *34*), a possible role of RIPK1 in mediating the wide presence of axonal degeneration in different neurodegenerative diseases should be considered.

REFERENCES AND NOTES

1. E. Beeldman *et al.*, *Amyotroph. Lateral Scler. Frontotemporal Degener.* **16**, 410–411 (2015).
2. E. T. Cirulli *et al.*, *Science* **347**, 1436–1441 (2015).
3. H. Maruyama *et al.*, *Nature* **465**, 223–226 (2010).
4. I. Munitic *et al.*, *J. Immunol.* **191**, 6231–6240 (2013).
5. G. Zhu, C. J. Wu, Y. Zhao, J. D. Ashwell, *Curr. Biol.* **17**, 1438–1443 (2007).
6. D. Ofengeim, J. Yuan, *Nat. Rev. Mol. Cell Biol.* **14**, 727–736 (2013).
7. S. He *et al.*, *Cell* **137**, 1100–1111 (2009).
8. L. Sun *et al.*, *Cell* **148**, 213–227 (2012).
9. D. W. Zhang *et al.*, *Science* **325**, 332–336 (2009).
10. A. Degterev *et al.*, *Nat. Chem. Biol.* **4**, 313–321 (2008).
11. A. Degterev *et al.*, *Nat. Chem. Biol.* **1**, 112–119 (2005).
12. L. Conforti, J. Gilley, M. P. Coleman, *Nat. Rev. Neurosci.* **15**, 394–409 (2014).
13. M. C. Raff, A. V. Whitmore, J. T. Finn, *Science* **296**, 868–871 (2002).
14. J. T. Wang, Z. A. Medress, B. A. Barres, *J. Cell Biol.* **196**, 7–18 (2012).
15. S. Sasaki, S. Maruyama, *J. Neurol. Sci.* **110**, 114–120 (1992).
16. L. Zhuo *et al.*, *Genesis* **31**, 85–94 (2001).
17. B. E. Clausen, C. Burkhardt, W. Reith, R. Renkawitz, I. Förster, *Transgenic Res.* **8**, 265–277 (1999).
18. C. Lappe-Siefke *et al.*, *Nat. Genet.* **33**, 366–374 (2003).
19. C. N. Parkhurst *et al.*, *Cell* **155**, 1596–1609 (2013).
20. D. E. Christofferson, J. Yuan, *Curr. Opin. Cell Biol.* **22**, 263–268 (2010).
21. J. Hitomi *et al.*, *Cell* **135**, 1311–1323 (2008).
22. D. E. Christofferson *et al.*, *Cell Death Dis.* **3**, e320 (2012).
23. A. Polykratis *et al.*, *J. Immunol.* **193**, 1539–1543 (2014).
24. D. Ofengeim *et al.*, *Cell Rep.* **10**, 1836–1849 (2015).
25. P. Langfelder, S. Horvath, *BMC Bioinformatics* **9**, 559 (2008).
26. K. A. Kigerl *et al.*, *J. Neurosci.* **29**, 13435–13444 (2009).
27. A. Subramanian *et al.*, *Proc. Natl. Acad. Sci. U.S.A.* **102**, 15545–15550 (2005).
28. S. I. Berger, J. M. Posner, A. Ma'ayan, *BMC Bioinformatics* **8**, 372 (2007).
29. S. H. Kang *et al.*, *Nat. Neurosci.* **16**, 571–579 (2013).
30. D. B. Re *et al.*, *Neuron* **81**, 1001–1008 (2014).
31. T. W. Gould *et al.*, *J. Neurosci.* **26**, 8774–8786 (2006).
32. J. J. Peschon *et al.*, *J. Immunol.* **160**, 943–952 (1998).
33. T. Osawa *et al.*, *Neuropathology* **31**, 569–574 (2011).
34. H.-X. Deng *et al.*, *Arch. Neurol.* **68**, 1057–1061 (2011).

ACKNOWLEDGMENTS

We thank B. Caldarone of the NeuroBehavior Laboratory, Harvard Institute of Medicine, for conducting mouse behavior analysis; J. Walters at the Harvard Medical School Nikon microscope facility for fluorescence microscopy; and M. Ericsson of the Electron Microscopy Facility at Harvard Medical School for analysis. This work was supported in part by grants from the National Institute of Neurological Disorders and Stroke (1R01NS082257) and the National Institute on Aging (1R01AG047231), NIH; and by the National Science and Technology Major Project of China (2014ZX09102001-002) and State Key Program of National Natural Science of China (no. 31530041) (to J.Y.); National Institute of Allergy and Infectious Diseases (2RO1AI075118) (to M.A.K.); European Research Council Advanced Grants (grant agreement no. 323040) (to M.P.) and Target ALS (to J.R.). Y.I. was supported in part by postdoctoral fellowships from Japan (Daiichi Sankyo Foundation of Life Science, The Nakatomi Foundation, the Mochida Memorial Foundation for Medical and Pharmaceutical Research, and Japan Society for the Promotion of Science). D.O. was supported by a postdoctoral fellowship from the National Multiple Sclerosis Society and a National Multiple Sclerosis Society Career Transition Award. H.C. was supported by a grant from Huazhong University of Science and Technology, Wuhan, China. $Ripk3^{-/-}$ mice and K48 ubiquitin antibodies are available from V. Dixit under a material transfer agreement with Genentech. $Ripk1^{D138N}$ mice are available from M. Pasparakis of University of Cologne, Germany, under a material transfer agreement with University of Cologne. J.Y. is an inventor on U.S. patent 7,491,743 B2 held by Harvard University that covers 7-Cl-O-Nec-1.

SUPPLEMENTARY MATERIALS

www.sciencemag.org/content/353/6299/603/suppl/DC1
Materials and Methods
Figs. S1 to S8
Tables S1 to S4
References (*35*–*40*)

13 March 2016; accepted 7 July 2016
10.1126/science.aaf6803

RIPK1 mediates axonal degeneration by promoting inflammation and necroptosis in ALS
Yasushi Ito, Dimitry Ofengeim, Ayaz Najafov, Sudeshna Das, Shahram Saberi, Ying Li, Junichi Hitomi, Hong Zhu, Hongbo Chen, Lior Mayo, Jiefei Geng, Palak Amin, Judy Park DeWitt, Adnan Kasim Mookhtiar, Marcus Florez, Amanda Tomie Ouchida, Jian-bing Fan, Manolis Pasparakis, Michelle A. Kelliher, John Ravits and Junying Yuan (August 4, 2016)
Science **353** (6299), 603-608. [doi: 10.1126/science.aaf6803]

Editor's Summary

Axonal pathology and necroptosis in ALS

Necroptosis, a non–caspase-dependent form of cell death, can be reduced in disease states by inhibiting a kinase called RIPK1. Until now, no human mutations have been linked to necroptosis. Ito *et al.* show that loss of optineurin, which is encoded by a gene that has been implicated in the human neurodegenerative disorder ALS (amyotrophic lateral sclerosis), results in sensitivity to necroptosis and axonal degeneration. When RIPK1-kinase dependent signaling is disrupted in mice that lack optineurin, necroptosis is inhibited and axonal pathology is reversed.

Science, this issue p. 603

Science (print ISSN 0036-8075; online ISSN 1095-9203) is published weekly, except the last week in December, by the American Association for the Advancement of Science, 1200 New York Avenue NW, Washington, DC 20005.

www.sciencemag.org/content/353/6299/604/suppl/DC1

Supplementary Materials for

RIPK1 mediates axonal degeneration by promoting inflammation and necroptosis in ALS

Yasushi Ito, Dimitry Ofengeim, Ayaz Najafov, Sudeshna Das, Shahram Saberi, Ying Li, Junichi Hitomi, Hong Zhu, Hongbo Chen, Lior Mayo, Jiefei Geng, Palak Amin, Judy Park DeWitt, Adnan Kasim Mookhtiar, Marcus Florez, Amanda Tomie Ouchida, Jian-bing Fan, Manolis Pasparakis, Michelle A. Kelliher, John Ravits, Junying Yuan*

*Corresponding author. Email: jyuan@hms.harvard.edu

Published 5 August 2016, *Science* **353**, 604 (2016)
DOI: 10.1126/science.aaf6803

This PDF file includes

www.sciencemag.org/content/353/6299/604/suppl/DC1

Supplementary Materials for

RIPK1 mediates axonal degeneration by promoting inflammation and necroptosis in ALS

Yasushi Ito, Dimitry Ofengeim, Ayaz Najafov, Sudeshna Das, Shahram Saberi, Ying Li, Junichi Hitomi, Hong Zhu, Hongbo Chen, Lior Mayo, Jiefei Geng, Palak Amin, Judy Park DeWitt, Adnan Kasim Mookhtiar, Marcus Florez, Amanda Tomie Ouchida, Jian-bing Fan, Manolis Pasparakis, Michelle A. Kelliher, John Ravits, Junying Yuan*

*Corresponding author. Email: jyuan@hms.harvard.edu

Published 5 August 2016, *Science* **353**, 604 (2016)
DOI: 10.1126/science.aaf6803

This PDF file includes

Supplementary Information

Author contributions

YI and JY conceived the concept and designed the experiments. YI performed majority of experiments. DO advised YI in many experiments. SD did bioinformatics analysis. SS and JR provided human pathological samples. AN, YL, JH, HZ, HC, LM, JG, PA, JPD, AKM, MF, ATO and JF assisted experiments. MK and MP provided *Ripk1*$^{D138N/D138N}$ mice. JY coordinated the study. JY, YI and DO wrote the manuscript.

Materials and Methods

Animals

Optn$^{tm1a(EUCOMM)Wtsi}$ (MASV; EPD0116_2_G06) mice were from Wellcome Trust Sanger Institute, UK. Optn$^{tm1a(EUCOMM)Wtsi}$ (MASV; EPD0116_2_G06) were crossed with B6.129S4-*Gt(ROSA)26Sor*$^{tm1(FLP1)Dym}$/RainJ mice to remove the FRT cassette including both neo and LacZ to generate a conditional ready allele (*Optn*$^{F/F}$). *Optn*$^{F/F}$ mice were crossed with CMV-cre mice to generate *Optn*-/- mice. *Optn*-/- mice and *Optn*$^{F/F}$ mice were backcrossed with C57B6 mice (Jackson laboratory) for 10 generations. *Ripk3*$^{-/-}$ mice were kindly provided by Dr. Vishva Dixit of Genentech *(35)*. *CNP-cre* mice were kindly provided by Brian Popko of University of Chicago and Klaus Nave Max Planck Institute for Experimental Medicine, Germany *(18)*. CMV-cre mice [B6.C-Tg(CMV-cre)1Cgn/J; Stock No: 006054], [B6.129P2- Lyz2tm1(cre)Ifo/J; Stock No:004781], GFAP-cre [B6.Cg-Tg(Gfap-cre)73.12Mvs/J; Stock No: 012886], Mnx1-cre [B6.129S1-Mnx1tm4(cre)Tmj/J/J; Stock No: 006600], Cx3cr1-cre mice [B6.129P2(Cg)-Cx3cr1 $^{tm2.1(cre/ERT2)Litt}$/WganJ/J; Stock No: 021160], SOD1-G93A mice [B6SJL-Tg(SOD1G93A)1Gur/J; Stock No:002726] and C57BL/6 (B6) mice were obtained from Jackson Laboratory. In order to examine the expression of Lyz2 driven cre recombinase (B6.129P2-Lyz2<tm1(cre)Ifo>/J – 004781), mice with two copies of this cre recombinase and tdTomato reporter mouse (B6.Cg-Gt(ROSA)26Sortm14(CAG-tdTomato)Hze/J were generated. We examined the expression of Lyz2- recombinase in microglial cells in the murine spinal cord by colocalizing the tdTomato signal with IBA1

immunostaining. All animals were maintained in a pathogen-free environment, and experiments on mice were conducted according to the protocols approved by the Harvard Medical School Animal Care Committee.

Human tissues

The research involving control and ALS human pathological samples was approved by the Institutional Review Board (IRB) of Harvard University.

Mouse genotyping

Optn genotyping used following primers (5'>3'):

CAS_R1_Term (for FRT cassette): TCGTGGTATCGTTATGCGCC.

Optn_47570_F: ACCACACGATGGCTCACAAC

Optn_47570_R: GTGTCTCAAAACAACAAATTCTCCC

Other mouse genotyping protocols followed the published literatures.

Nec-1s administration

The method of Nec-1s formulation and delivery was as described in *(24)*. Custom synthesized Nec-1s was first dissolved in DMSO (50% w/v), and then transferred into 35% PEG solution and this was suspended in water containing 2% sucrose. Mice were provided with vehicle control and Nec-1s as drinking water ad lib. Each mouse drank vehicle or Nec-1s containing water about 5-10 mL/day (Nec-1s=2.5-5 mg/day).

Open Field Activity Test

The animal behavior study was conducted by the NeuroBehavior Laboratory, Harvard Institute of Medicine. The mouse genotypes were blinded to the testers. The open field test was used to study behavioral responses of mice that were confined to a novel arena. The test arena was made of Plexiglas and consists of a square base with walls 20-40cm high. All walls were clear but opaque barriers were added between arenas to hinder the subjects' ability to see one another during testing. For each testing session, the animal was allowed free exploration in the environment for a maximum of 1 hr. During the session only, the animal did not have access to food or water. A computer-assisted infra-

red tracking system was used to record the number of beam breaks (activity) and user defined zone entries. Vertical count = Rearing behavior (i.e. animal on hind legs causing a break in the IR beams that measure Z-axis movement). Block No=5 min block of time (1-12=5min-60min). Zone=Zone animal is in (0=periphery; 1=Center). The data were analyzed with ANOVA followed by Fisher's PLSD test.

Neurological scoring system of *SOD1*^{G93A} mice followed the guideline provided by the Jackson Laboratory (http://www.researchals.org/uploaded_files/p4l_jax_sod1manual_20091202_29aPcx.pdf) . Score of 0: Full extension of hind legs away from lateral midline when mouse is suspended by its tail, and mouse can hold this for two seconds, suspended two to three times. Score of 1: Collapse of leg extension towards lateral midline (weakness) during tail suspension. Score of 2: Toes curl under at least twice during walking of 12 inches, or any part of foot is dragging along cage bottom/table. Score of 3: Rigid paralysis or minimal joint movement, foot not being used for generating forward motion. Score of 4: Mouse cannot right itself within 30 seconds after being placed on either side.Mice reached score 2 are considered to have onset.

ELISA

Spinal cord was homogenized in 1% Triton X-100 in PBS supplemented with Complete Protease Inhibitor (Roche, Indianapolis, IN, USA). Total protein levels were determined by Bradford protein assay (Bio-Rad, Hercules, CA, USA). The levels of TNFα, IL-6, and IL-1β in the spinal cord were determined using the appropriate ELISA kit according to the manufacturers instructions (R&D Systems, Minneapolis, MN, USA).

Histology and immunochemistry

Animals were sacrificed and perfused with PBS followed by 4% paraformaldehyde. The lumbar regions of the spinal cord were dissected and 16-μm spinal cord cross-sections were prepared on a cryostat. For immunostaining, tissue sections were mounted and blocked with 10% normal goat serum and 1% BSA, and then incubated with primary antibodies at 4°C overnight. Images were collected with a Nikon Ti-E confocal microscope equipped with A1R scan head with spectral detector and resonant scanners;

images were acquired with Nikon elements software. For each image point, z-series optical sections were collected with a step size of 0.2 microns, using a Prior Proscan focus motor. Gamma, brightness, and contrast were adjusted on displayed images (identically for compared image sets) using FIJI software.

Antibodies

Optn (Cayman, Cat#100000, Santa Cruz, Cat#sc48903, snd Abcam, Cat#ab23666), RIPK1 (BD, Cat#610459, and Cell Signaling, Cat# #3493), p-S14/15 RIPK1 (Cell Signaling), anti-K48 ubiquitin ab (Genentech), SMI32 (Calbiochem, Cat#NE1023), CC1 (Calbiochem, Cat#OP80), GFAP (Invitrogen, Cat#130300), Iba-1 (Abcam, Cat#ab107159, and Wako, Cat#019-19741), RIPK3 (Abcam, Cat#ab72106, Cell Signaling, and Serotec, Cat#AHP1797), MLKL (Abcam, Cat#ab172868 and ab183770, and Sigma, Cat#SAB1302339), p-MLKL (Abcam, Cat# ab187091 and ab196436), FADD (Abcam, Cat#ab124812, and Santa Cruz, Cat#sc6036), K48 (Genentech), SP1 (Santa Cruz, Cat#sc14027), 2H3 (the Developmental Studies Hybridoma Bank, Cat#3272160), SV2 (the Developmental Studies Hybridoma Bank, Cat#2579958) and β-actin (Santa Cruz, Cat#sc81178). We thank Dr. Gary Kasof of Cell Signaling for developing phospho-S14/15 RIPK1 antibody and Dr. Vishva Dixit of Genentech for anti-K48 ubiquitin ab.

Transmission electron microscopy

Animals were sacrificed and perfused with PBS followed by fixation solution of 2.5% glutaraldehyde/2% paraformaldehyde in 0.1 M sodium cacodylate buffer (pH 7.4). Small pieces (1-2mm^3 cubes) of lumbar spinal cords (L1-L4) and the associated ventral roots from a perfusion fixed animal were post-fixed for at least 2 hrs at RT in the above fixative, washed in 0.1M cacodylate buffer and postfixed with 1% osmiumtetroxide (OsO4)/1.5% potassium ferrocyanide (KFeCN6) for 1 hr, washed in water 3x and incubated in 1% aqueous uranyl acetate for 1hr, followed by 2 washes in water and subsequent dehydration in grades of alcohol (10min each; 50%, 70%, 90%, 2x10min 100%). The samples were then put in propyleneoxide for 1 hr and infiltrated ON in a 1:1 mixture of propyleneoxide and TAAB Epon (Marivac Canada Inc. St. Laurent, Canada).

The following day the samples were embedded in TAAB Epon and polymerized at 60 degrees C for 48 hrs. Ultrathin sections (60nm) were cut with a Reichert Ultracut-S microtome, picked up on to copper grids stained with lead citrate and examined in a JEOL 1200EX Transmission electron microscope or a TecnaiG^2 Spirit BioTWIN and images were recorded with an AMT 2k CCD camera. Myelination, axonal morphology and g-ratios of different genotypes were determined from counting of ~200 axons in the ventrolateral lumbar spinal cord white matter of 3 mice of each genotype at 3 months of age using ImageJ analysis.

Motor neuron counting

The numbers of motor neurons in the lumbar spinal cords (L1-L4) from mice 12 weeks and 2 years of age were determined. A total of 4 sections (16 μm) (one each for L1-L4) from 5 mice for each genotype were immunostained with motor neuron marker SMI32, imaged using fluorescence microscopy and counted using ImageJ.

Characterization of neuromuscular junctions

Tibialis anterior muscles from mice at 12 weeks of age were dissected, pinned in mild stretch and immersion-fixed for 30 min in 4% paraformaldehyde at RT. Fixed muscles were cryoprotected in 30% sucrose/phosphate-buffered saline (48 hrs at 4C). 100-μm thick frozen sections were cut longitudinally through the entire muscle. Sections were incubated overnight at RT in a cocktail of primary antibodies with anti-neurofilament 2H3 (1:250) and anti-SV2 (1:250), in PBS, 0.3% TritonX100, 3% BSA. Sections were washed and incubated overnight with an Alexa-Fluor-488 conjugated anti-mouse IgG1 and Alexa-Fluor-594 conjugated α-bungarotoxin (Invitrogen), each at a 1:1000 dilution in the same buffer as above. Sections were then mounted in fluorescence mounting medium and imaged using fluorescence microscopy at 40x magnification and analyzed using ImageJ. The data were obtained from analyzing ~200 NMJs from 3 mice of each genotype (12 weeks old).

TUNEL

TUNEL assay was used to detect dead cells with DNA fragmentation using In Situ Cell Death Detection Kit, POD (Roche) by following manufacture's protocol.

Axonal diameter and G ratio determination

The axonal diameters were measured on EM images using ImageJ. G-ratio was determined as the ratio of inner axonal diameter to the total outer diameter of each axon fiber. ~200 axons from the ventral lateral white matter of lumbar spinal cords (L1-L4, one section each) of 3 mice (12 weeks old) were measured in each analysis.

Primary microglia and oligodendrocyte culture

Primary oligodendrocyte and microglial cultures were prepared as described previously *(36)*. Briefly, forebrains of 1 to 2-d-old mouse pups were digested with 0.01% trypsin and triturated with DMEM containing 10% heat-inactivated fetal bovine serum and 1% penicillin-streptomycin. Dissociated cells were plated onto poly-d-lysine coated 75cm^2 flasks and fed every 3d for 7-10 days. Following an initial 1 hr shake of the culture, microglia were collected and cultured in DMEM+10%FBS. The quality of purification was analyzed by FCS using CD11b as a marker for microglia (>90% CD11b+). RNA preparation and library generation followed the protocol from the manufacturer's protocol from Illumina.

For oligodendrocyte culture, the flasks were continued shaken overnight at 200 rpm to collect oligodendrocytes. The cells were then plated onto poly-lysine-coated culture plates, and maintained in a basal defined medium (BDM, 0.1% bovine serum albumin, 50 μg/ml human apo-transferrin, 50 μg/ml insulin, 30 nM sodium selenite, 10 nM D-biotin and 10 nM hydrocortisone in DMEM) for 5-9 days at 37°C in a humid atmosphere of 5% CO2 and 95% air. Half of the culture medium was replaced with fresh media every other day, and cells were harvested between DIV7-9. Around 60-85% of cells were of oligodendrocyte lineage (i.e. either Olig2, O4, or MBP positive), the remainder were astrocytes and microglia. Cells were maintained for 10-14 days *in vitro*. For cell death assays, cells were treated with TNFα (50 ng/mL) for 24 h and viability was assessed using Toxilight assay (Lonza), which measures the release of adenylate kinase (AK) from dead cells into the media.

Primary astrocyte culture

Mixed glia was prepared as described [37, 38], and cultured until confluent (day 7-10). The cells were then incubated with 0.02 mg/ml of Clodronate encapsulated liposomes (Clodrosome) (Encapsula NanoSciences LLC) for 2-3 days, washed, and the astrocyte monolayer was separated using mild trypsinization procedure, and plated. Cells were >99% astrocytes, as determined by staining with GFAP or GLAST, with less than 1% contamination of CD11b+ microglia cells (data not shown).

FACS sorting of astrocytes

Isolated CNS cells were purified by cell sorting using FACSAria I (BD Bioscience) as previously described *(38)* with minor modifications. Briefly, cells were sorted in the presence of 7-AAD for the exclusion of nonviable cells, and Hoechst 33342 dye for nuclear visualization, and astrocytes were isolated following depletion of microglia, monocytes, oligodendrocytes, endothelial cells, and lymphocytes (T-cells, B-cells, and NK cells).

Cell culture

L929 cells were cultured in DMEM supplemented with 10% FBS and penicillin and streptomycin.

Western blotting for p-RIPK1

Triton X-114 fractionation experiments were performed according to Wang et al. *(39)* with some modification. Briefly, cells were lyzed in 20 mM HEPES, pH 7.4, 150mM NaCl, 2% Triton X-114, 1 mM benzamidine, 1 mM PMSF and Complete protease inhibitor (Roche) and incubated on ice for 30 min. The lysates were centrifuged at 16,000×g for 15min at 4C. Supernatants were incubated at 30°C for 3 min and spun at 1,500×g for 5 min at room temperature. The detergent fraction was diluted with PBS and re-centrifuged at 1,500×g for 5 min at RT. 5X SDS-PAGE sample buffer was added to the resulting detergent fraction and samples were resolved on 10% SDS-PAGE gels.

Generation and immortalization of MEFs

Optn+/- male and female mice were crossed and the pregnancy was terminated at E11-13 stage. Embryos were homogenized and treated with trypsin/EDTA, sieved through 70-micron filter and primary MEFs were cultured in high glucose DMEM supplemented with 15% FBS, non-essential amino acids, sodium pyruvate, penicillin, streptomycin and amphotericin B. At passages 4-6, primary MEFs were immortalized by transfection with SV40 small + large T antigen-expressing plasmid (Addgene 22298) using Lipofectamine 2000.

Statistics and Bioinformatics

Multiple comparisons were statistically evaluated using a two-tailed Student's *t*-test. Differences were considered statistically significant if $p<0.05$(*); $p<0.01$ (**) or $p<0.001$(***). Data are expressed as the mean ± standard error of the mean (SEM). Pairwise comparisons between two groups were performed using the Student's t-test. For multiple comparisons with the three genotypes, we performed one-way Anova. Two-way Anova was performed for multiple comparisons with genotypes and ages, and the results obtained by standard least squares fits followed by appropriate post hoc tests are shown.

Co-expression analysis to identify modules was performed using the WGCNA package *(25)* in R version 3.2.0. The heatmaps were generated using the heatmap function in the stats library. Transcription factor identification was performed using the MSigDB (Molecular Signatures Database) *(27)*, which performs hyper-geometric tests to compute significance of overlap between the gene set of interest and the gene lists in the database. The C3 gene set collection in MSigDb containing predicted transcription factor targets was used for this purpose *(40)*. Gene networks were created using the Gene2Network software *(28)*, which uses mammalian protein interactions databases to identify other genes that are significantly connected to the input seed list.

Supplementary Figure legends

Fig. S1. Generation of *Optn-/-* mice. (**A-B**) Genotyping of *Optn*-/- mice and western blotting analysis of different tissues from WT and *Optn*-/- mice to show the absence of OPTN expression in *Optn*-/- mice. (**C-D**) Immunostaining of motor neuron marker SMI32 (**C**) and quantification of SMI32+ motor neurons (**D**) in the ventral spinal cords of WT and *Optn*-/- mice at 12 weeks and 2 years of age using ImageJ. (**E-F**) Electron microscopic images (**E**) and quantification (**F**) of the motor axon myelination in the ventrolateral spinal cords of WT (*Optn*+/+) and *Optn*-/- mice at 3 weeks, 12 weeks and 2 years of age. * highlights dysmyelinated axons. # marks a degenerating axon. Note loose myelination and the presence of excess oligodendrocyte cytoplasm surrounding these axons in *Optn*-/- mice. (**G**-**J**) Electron microscopic analysis of the motor axons in the ventral roots of lumbar spinal cords from WT (*Optn*+/+) and *Optn*-/- mice (12 weeks old). The mean axonal numbers, mean g-ratios and mean axonal diameters (**H**), individual g-ratios distribution (**I**) and the distributions of axonal diameters (**J**) are shown. (**K**-**L**) Motor endplates are identified with a-bungarotoxin (red); axons are identified with neurofilament + SV2 (green). Images depict innervated endplates (yellow indicates overlap) in WT (*Optn*+/+), denervated endplates in *Optn*-/- mice (**K**) and quantitative analysis (**L**). Data are shown as % of endplates classified as innervated in *Optn*-/- muscle compared to that of WT (*Optn*+/+). 200 endplates were counted from 3 mice (12 weeks old) per genotype.

Fig. S2. Cell-type specific deletion of OPTN expression in *Optn$^{F/F}$; Lyz2-cre, Optn$^{F/F}$; Cnp-cre*, and *Optn$^{F/F}$; Gfap-cre* mice. (**A**) Primary microglia isolated from newborn *Optn$^{F/F}$* or *Optn$^{F/F}$; Lyz2-cre* mice were analyzed by western blotting using anti-OPTN and anti-b-actin. (**B**) The expression of Lyz2-directed tdTomato in Iba1+ microglia in the spinal cords. Sections of the ventral spinal cords from mice with indicated genotypes were immunostained with IBA1. (**C**-**D**) Sections of the ventral spinal cords from mice with indicated genotypes were double-immunostained with IBA1 for CC1 and OPTN for *Optn$^{F/F}$; Cnp-cre* mice (**C**) or GFAP and OPTN for *Optn$^{F/F}$; GFAP-cre* mice (**D**). (**E-F**) Primary astrocytes were isolated from newborn *Optn$^{F/F}$*or *Optn$^{F/F}$; GFAP-cre* mice and

analyzed by western blotting (**E**) and qRT-PCR for Optn (**F**). (**G**) Astrocytes were isolated from adult *Optn*$^{F/F}$, *Optn*$^{F/F}$*; GFAP-cre*, or *Optn*-/- mice (12 weeks old) by FACS and analyzed by qRT-PCR. *Optn*-/- astrocytes were used as a positive control. The amount of Optn qRT-PCR products was displayed as a ratio to that of GAPDH from the astrocytes of same genotype (**F**-**G**).

Fig. S3. Inducible deletion of OPTN from microglia leads to axonal pathology. (**A**) Western blotting analysis of microglia isolated from mice of indicated genotypes and treated with 4-hydroxy tamoxifen (TAM) (10 μg/ml) for 36 hrs. The expression of OPTN was analyzed by western blotting using indicated abs. (**B**) Electron microscopic analysis of the motor axonal myelination in the ventrolateral lumbar spinal cords from mice of indicated genotypes after the treatment of tamoxifen. Each mouse received tamoxifen (75 mg/kg/day) by subcutaneous injection every 24 hrs for one month starting from 8 weeks of age. (**C-E**) The mean axonal numbers, mean g-ratios and mean axonal diameters (**C**), individual g-ratios distribution (**D**) and the distributions of axonal diameters (**E**) in the ventrolateral lumbar spinal cord white matter (L1-L4) of mice with indicated genotype after induction of OPTN loss by tamoxifen.

Fig. S4. OPTN deficiency sensitizes cells to necroptosis. (**A**) Viability of L929 cells transfected with control non-targeting siRNA or 4 different siRNAs against OPTN for 48 hrs and then treated with zVAD.fmk (20 μM) or mTNFα (10 ng/ml) in the presence or absence of Nec-1s (10 μM) for another 24 hrs. (**B**) Viability of L929 cells transfected with control non-targeting siRNA, or OPTN siRNA, with or without siRNA targeting RIPK3 for 48 hrs and then treated with mTNFα (10 ng/ml) or Nec-1s (10 μM) for another 24 hrs as indicated. The knockdown controls are shown on the right side of each panel. (**C**) WT (*Optn*+/+*; Ripk3*+/+), *Optn*-/-*; Ripk3*+/+, *Optn*+/+; *Ripk3*-/- and *Optn*-/-*; Ripk3*-/- MEFs were treated with mTNFα (30 ng/ml), CHX (1 μg/ml) and zVAD.fmk (20 μM) (TCZ) with or without Nec-1s (10 μM) as indicated for 12 hrs. The cell viability in (**A**-**C**) was determined using CellTiterGro (Promega). (**D**) WT (*Optn*+/+) and *Optn*-/- MEFs were treated with TCZ as in (**D**) for indicated period of times. Anti-FADD ab was

used to immunoprecipitate complex IIb and the immunocomplex was analyzed by western blotting using indicated abs. b-actin was used as a loading control.

Fig. S5. Activation of inflammatory response in *Optn*-/- microglia. (**A**) Increased levels of TNFα production in isolated *Optn*-/- microglia were inhibited by Nec-1s (10 μM). (**B**) The spinal cords of *Optn*-/- and $Optn^{F/F}$*; Lyz2-cre* mice contained elevated levels of TNFα. The levels of TNFα were measured by ELISA. (**C**) The levels of Cd14 and Cd86 mRNA expression in *Optn*-/- with or without Nec-1s treatment (**left)** and *Optn*-/-; $Ripk1^{D138N/D138N}$ microglia (**right**) were determined by qRT-PCR. The levels of GAPDH were used as a control.

Fig. S6. The involvement of Sp1-mediated transcriptional response in mediating inflammation under OPTN deficient condition. (**A**) Network diagram of Sp1 target genes contained in module ME1. The seed list (Sp1 target genes in module ME1) is shown in red. Significantly connected genes are shown in yellow and other genes in grey. (**B**) L929 cells transfected with control non-targeting siRNA, or *Optn* siRNA, in the presence or absence of Nec-1s for 56 hrs. The levels of TNFα were measured in cell lysates by ELISA (left) and RT-PCR (right). (**C**) Viability of L929 cells transfected with control non-targeting siRNA, or OPTN siRNA, with or without siRNA targeting SP1, in the presence or absence of Nec-1s (10 μM) as indicated for 72 hrs. Cell viability was determined using CelltiterGro.

Fig. S7. Increased expression of RIPK1, RIPK3 and phosphor-MLKL in human sporadic cases of ALS. (**A**) Co-immunostaining of RIPK1 in human control and ALS spinal cord sections with markers for oligodendrocytes (CC1) (**bottom**) and microglia (Iba1) (**top**). Co-immunostaining of RIPK3 (**B**) and phosphor-MLKL (**C**) with CC1 as a marker for oligodendrocytes in the sections of the lateral column from lower spinal cord pathological samples of human control and ALS with CC1 as a marker for oligodendrocytes.

Fig. S8. A schematic diagram for the role of RIPK1 in mediating inflammation and necroptosis in spinal cords of ALS. OPTN suppresses the activation of RIPK1 by promoting its turnover in microglia to inhibit inflammatory response and in oligodendrocytes to suppress the activation of necroptosis.

Table S1. The z scores of Ripk1, Ripk3, Cyld and Optn in the genome-wide siRNA screen for regulators of necroptosis. Sensitization: z score ≤ -1.5. Inhibition: z score ≥ 1.5. Cyld is a positive control and knockdown of Cyld suppresses necroptosis.

Table S2. **Genes in ME1 module with highest connectivity**.

Table S3. Transcription factors whose targets are overrepresented in module ME1. The p-value of overlap with ME1 genes are computed using a hypergeometric test and False Discovery Rate (FDR q-values) are calculated with a Benjamini and Hochberg correction.

Table S4. The information on the pathological human samples used in this study.

Fig. S1

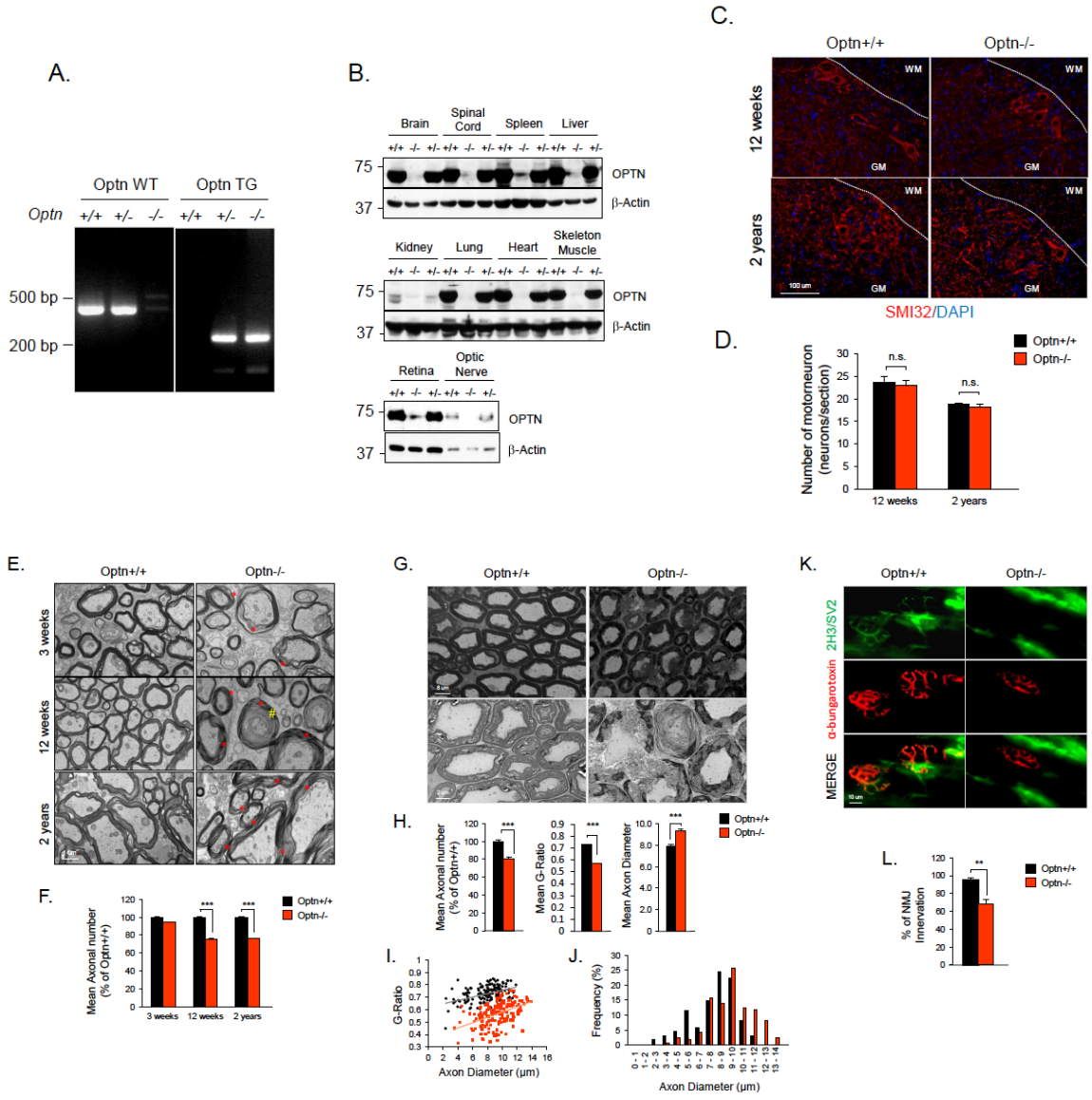
A.
Optn WT
Optn TG
Optn
+/+ +/- -/- +/+ +/- -/-
500 bp
200 bp
B.
Brain
Spinal Cord
Spleen
Liver
Kidney
Lung
Heart
Skeleton Muscle
Retina
Optic Nerve
75
37
OPTN
β-Actin
C.
Optn+/+
Optn-/-
12 weeks
2 years
WM
GM
SMI32/DAPI
D.
Number of motorneuron (neurons/section)
n.s.
12 weeks
2 years
Optn+/+
Optn-/-
E.
3 weeks
12 weeks
2 years
F.
Mean Axonal number (% of Optn+/+)
***
3 weeks
12 weeks
2 years
G.
H.
Mean Axonal number (% of Optn+/+)
Mean G-Ratio
Mean Axon Diameter
I.
G-Ratio
Axon Diameter (µm)
J.
Frequency (%)
Axon Diameter (µm)
K.
2H3/SV2
α-bungarotoxin
MERGE
L.
% of NMJ Innervation
**

Fig. S2

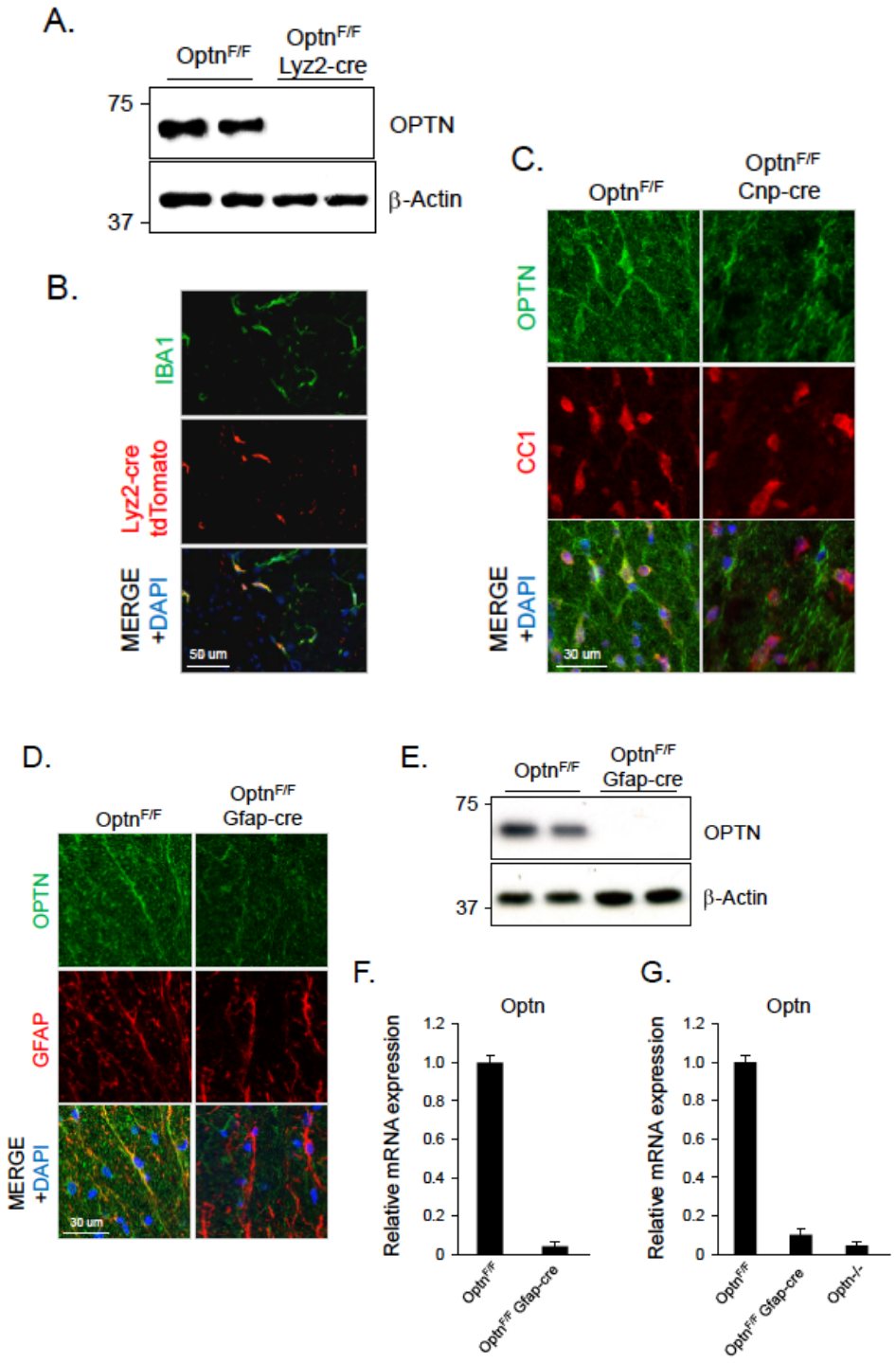
A.
Optn F/F
Optn F/F Lyz2-cre
75
OPTN
37
β-Actin
B.
IBA1
Lyz2-cre tdTomato
MERGE +DAPI
50 um
C.
Optn F/F
Optn F/F Cnp-cre
OPTN
CC1
MERGE +DAPI
30 um
D.
Optn F/F
Optn F/F Gfap-cre
OPTN
GFAP
MERGE +DAPI
30 um
E.
Optn F/F
Optn F/F Gfap-cre
75
OPTN
37
β-Actin
F.
Optn
Relative mRNA expression
1.2
1.0
0.8
0.6
0.4
0.2
0
Optn F/F
Optn F/F Gfap-cre
G.
Optn
Relative mRNA expression
1.2
1.0
0.8
0.6
0.4
0.2
0
Optn F/F
Optn F/F Gfap-cre
Optn-/-

Fig. S3

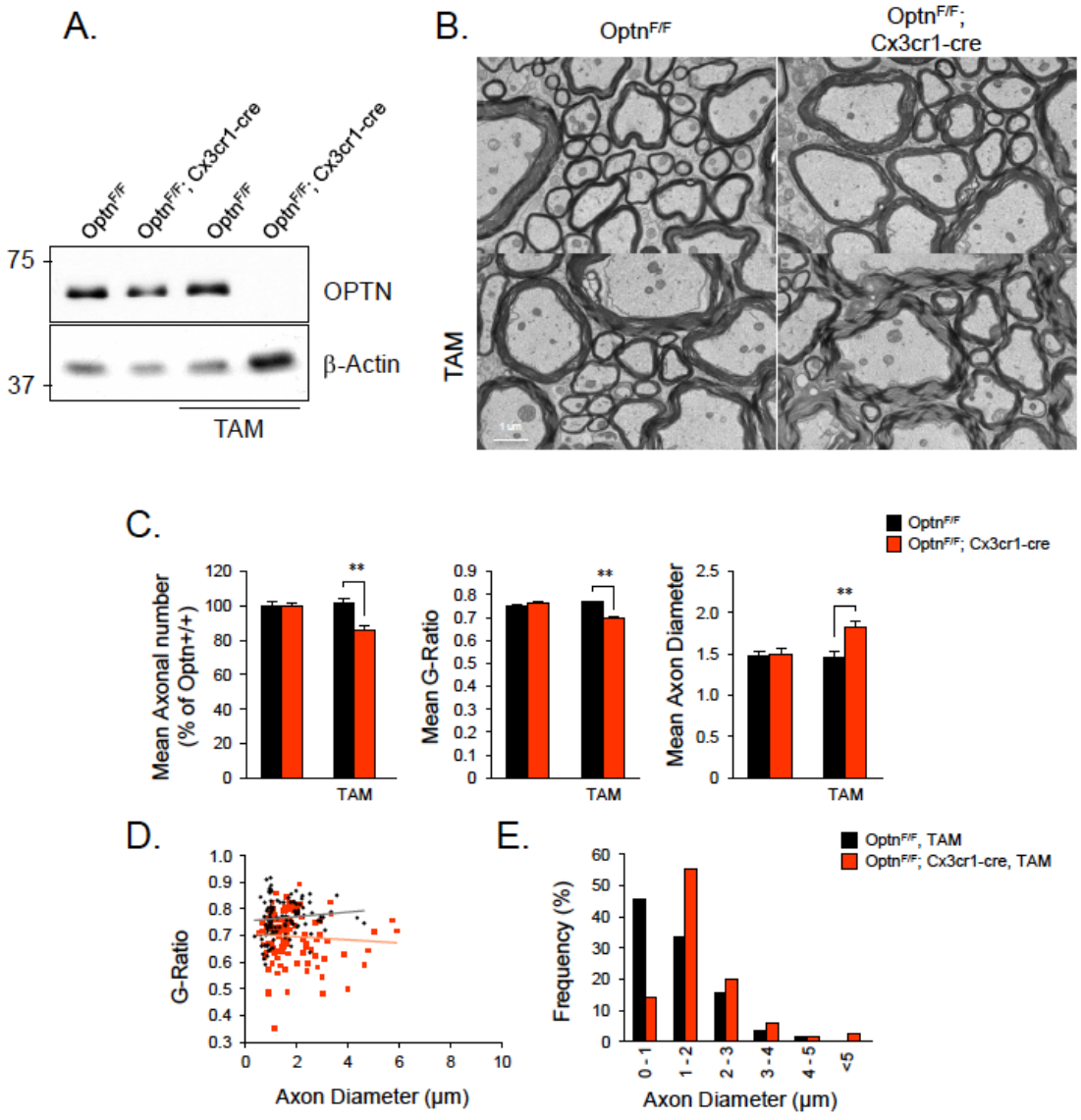
A.
Optn F/F
Optn F/F; Cx3cr1-cre
Optn F/F
Optn F/F; Cx3cr1-cre
75
37
OPTN
β-Actin
TAM
B.
Optn F/F
Optn F/F; Cx3cr1-cre
TAM
C.
Optn F/F
Optn F/F; Cx3cr1-cre
Mean Axonal number (% of Optn+/+)
Mean G-Ratio
Mean Axon Diameter
TAM
**
D.
G-Ratio
Axon Diameter (μm)
E.
Optn F/F, TAM
Optn F/F; Cx3cr1-cre, TAM
Frequency (%)
0 - 1
1 - 2
2 - 3
3 - 4
4 - 5
<5
Axon Diameter (μm)

Fig. S4

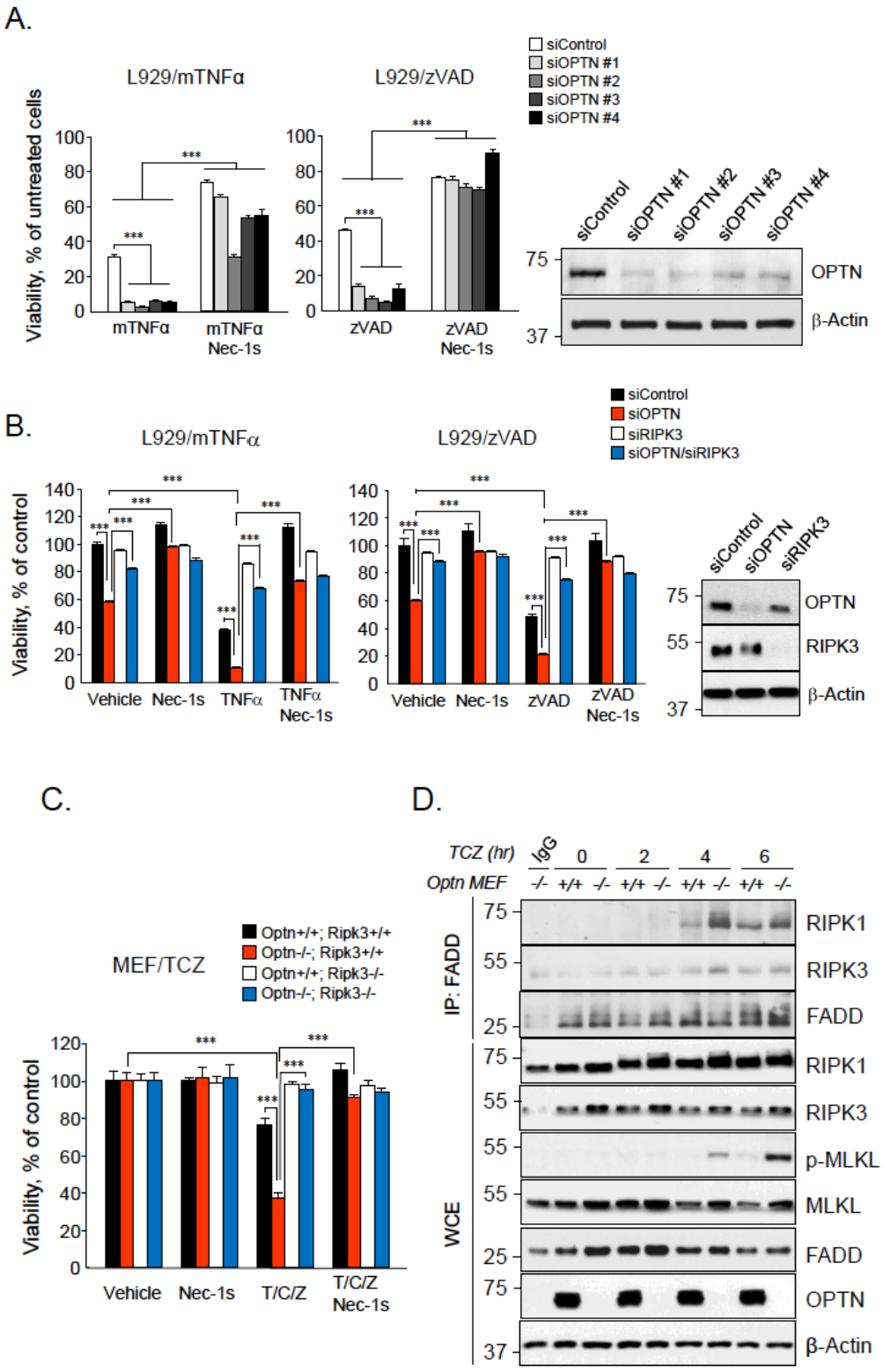
A.
L929/mTNFα
L929/zVAD
siControl
siOPTN #1
siOPTN #2
siOPTN #3
siOPTN #4
Viability, % of untreated cells
mTNFα
mTNFα Nec-1s
zVAD
zVAD Nec-1s
OPTN
β-Actin
B.
L929/mTNFα
L929/zVAD
siControl
siOPTN
siRIPK3
siOPTN/siRIPK3
Viability, % of control
Vehicle
Nec-1s
TNFα
TNFα Nec-1s
zVAD
zVAD Nec-1s
RIPK3
C.
MEF/TCZ
Optn+/+; Ripk3+/+
Optn-/-; Ripk3+/+
Optn+/+; Ripk3-/-
Optn-/-; Ripk3-/-
T/C/Z
T/C/Z Nec-1s
D.
TCZ (hr)
IgG
Optn MEF
IP: FADD
WCE
RIPK1
FADD
p-MLKL
MLKL

Fig. S5

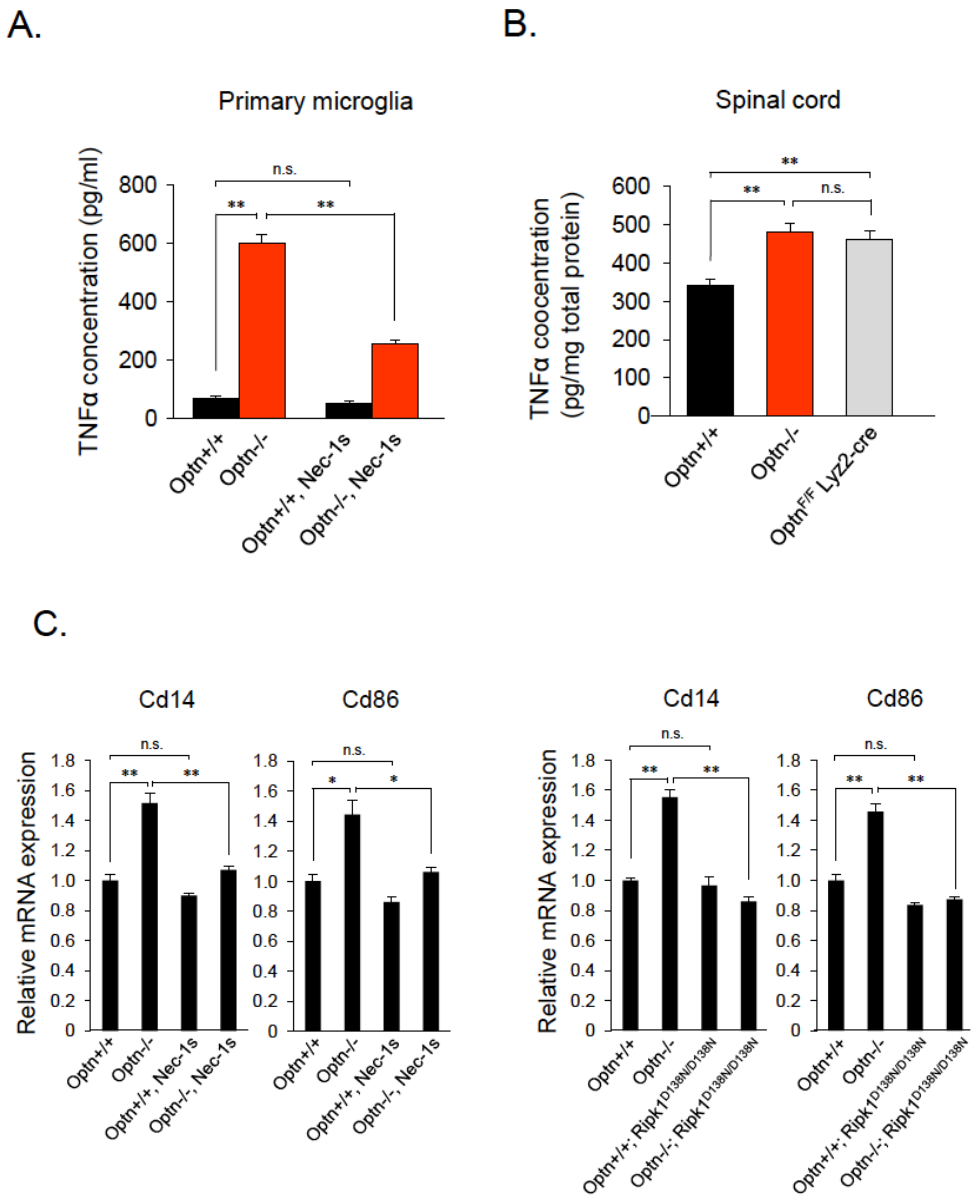
A.
Primary microglia
TNFα concentration (pg/ml)
800
600
400
200
0
n.s.
**
**
Optn+/+
Optn-/-
Optn+/+, Nec-1s
Optn-/-, Nec-1s
B.
Spinal cord
TNFα coocentration (pg/mg total protein)
600
500
400
300
200
100
0
**
**
n.s.
Optn+/+
Optn-/-
OptnF/F Lyz2-cre
C.
Cd14
Cd86
Relative mRNA expression
1.8
1.6
1.4
1.2
1.0
0.8
0.6
0.4
0.2
0
n.s.
**
**
*
*
Optn+/+
Optn-/-
Optn+/+, Nec-1s
Optn-/-, Nec-1s
Optn+/+, RipK1D138N/D138N
Optn-/-, RipK1D138N/D138N

Fig. S6

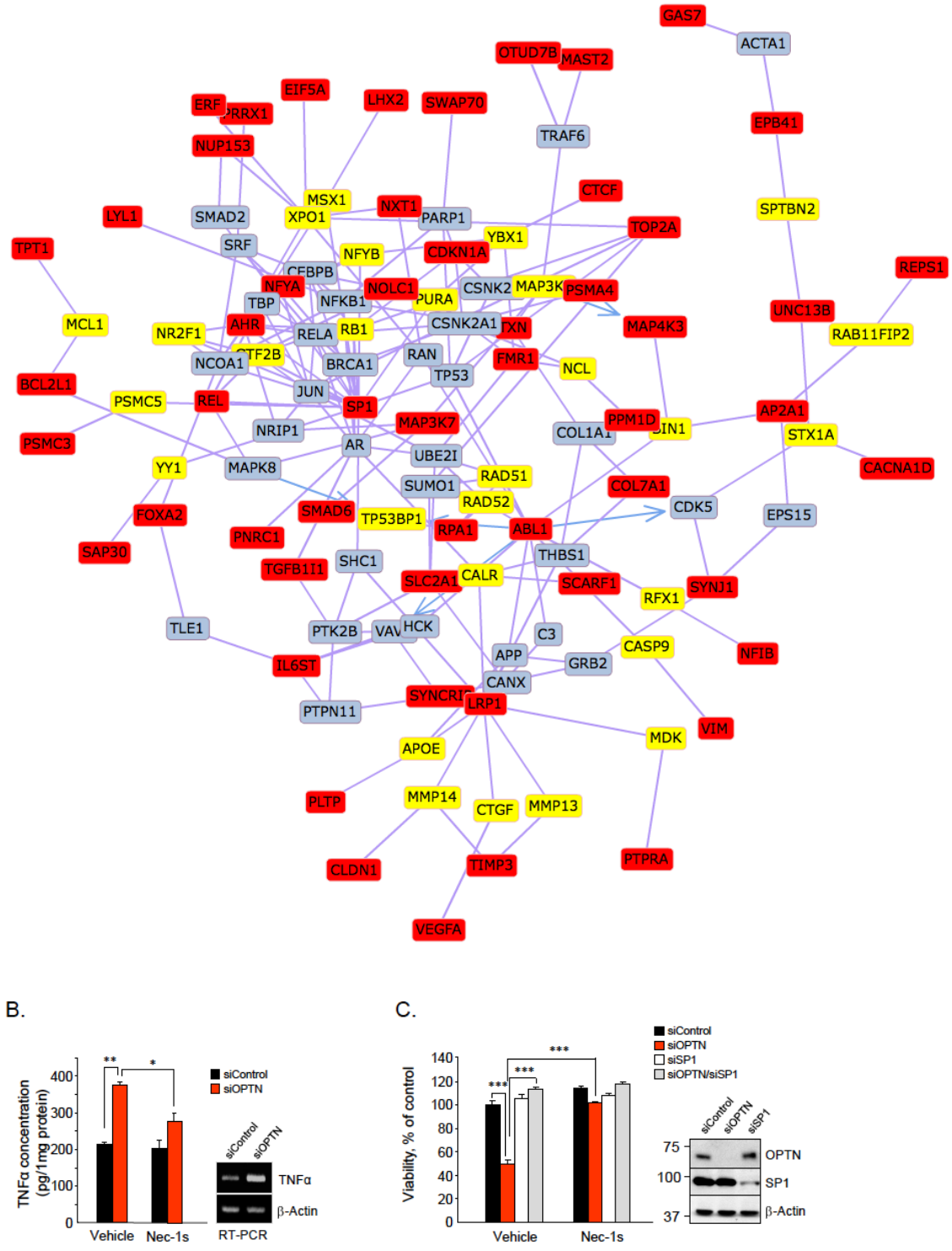
A.
GAS7
ACTA1
OTUD7B
MAST2
EIF5A
LHX2
SWAP70
ERF
PRRX1
TRAF6
EPB41
NUP153
CTCF
MSX1
NXT1
SPTBN2
LYL1
SMAD2
XPO1
PARP1
TOP2A
YBX1
TPT1
SRF
NFYB
CDKN1A
REPS1
CEBPB
NFYA
NOLC1
CSNK2
MAP3K
PSMA4
UNC13B
TBP
NFKB1
PURA
MCL1
AHR
CSNK2A1
TXN
MAP4K3
RAB11FIP2
NR2F1
RELA
RB1
NCOA1
BRCA1
RAN
FMR1
NCL
BCL2L1
TP53
JUN
PSMC5
REL
SP1
AP2A1
MAP3K7
PPM1D
NRIP1
COL1A1
JIN1
STX1A
PSMC3
AR
UBE2I
YY1
MAPK8
RAD51
CACNA1D
SUMO1
COL7A1
RAD52
CDK5
FOXA2
SMAD6
TP53BP1
EPS15
RPA1
ABL1
PNRC1
SAP30
THBS1
SHC1
TGFB1I1
SLC2A1
CALR
SCARF1
SYNJ1
RFX1
TLE1
PTK2B
VAV
HCK
C3
CASP9
NFIB
APP
GRB2
IL6ST
CANX
SYNCRIP
LRP1
PTPN11
VIM
MDK
APOE
PLTP
MMP14
CTGF
MMP13
PTPRA
CLDN1
TIMP3
VEGFA
B.
TNFα concentration (pg/1mg protein)
400
300
200
100
0
**
*
siControl
siOPTN
Vehicle
Nec-1s
siControl
siOPTN
TNFα
β-Actin
RT-PCR
C.
Viability, % of control
140
120
100
80
60
40
20
0
***
***
***
siControl
siOPTN
siSP1
siOPTN/siSP1
Vehicle
Nec-1s
siControl
siOPTN
siSP1
75
100
37
OPTN
SP1
β-Actin

Fig. S7

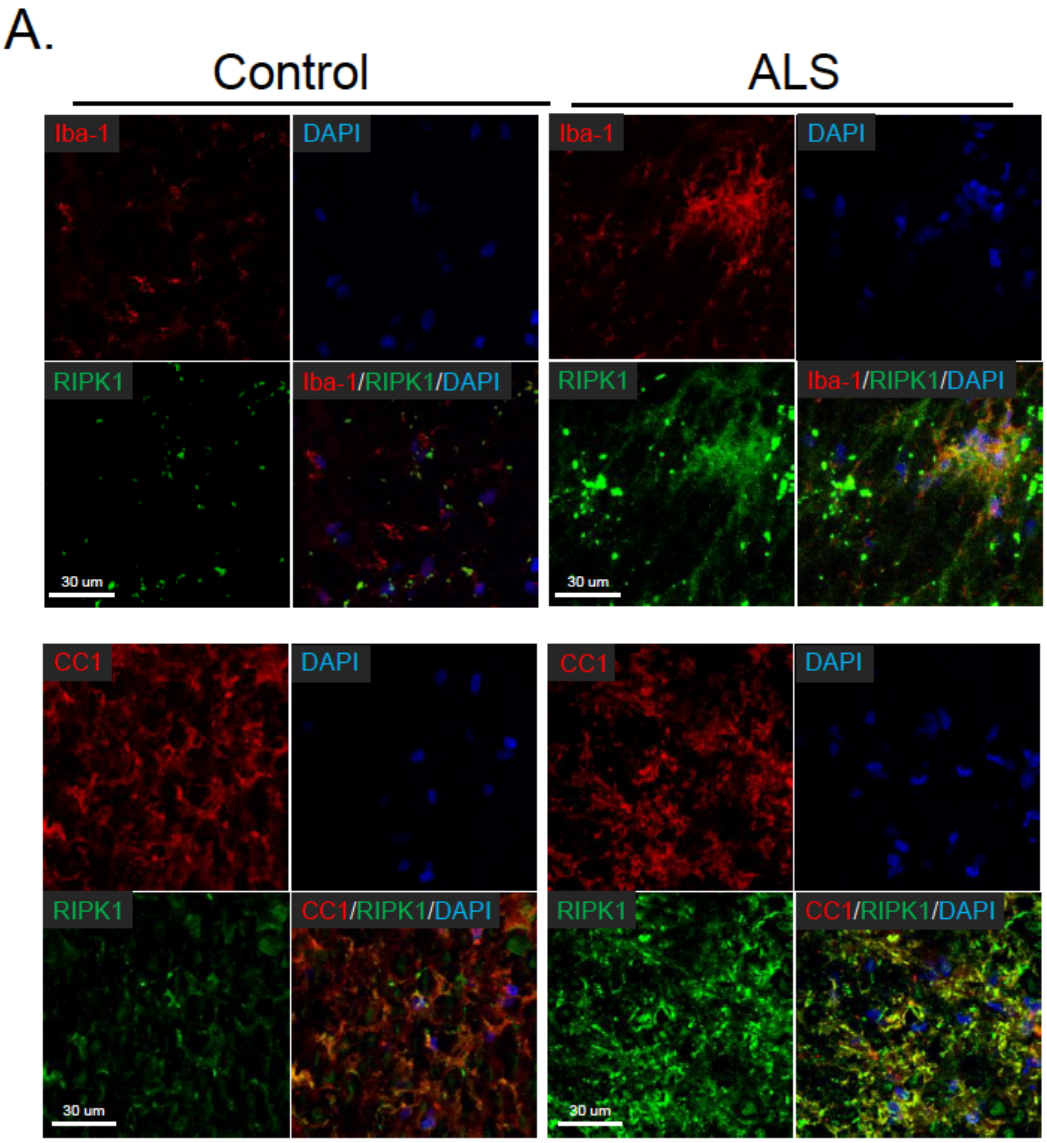
A.
Control
ALS
Iba-1
DAPI
RIPK1
Iba-1/RIPK1/DAPI
30 um
CC1
CC1/RIPK1/DAPI

B.

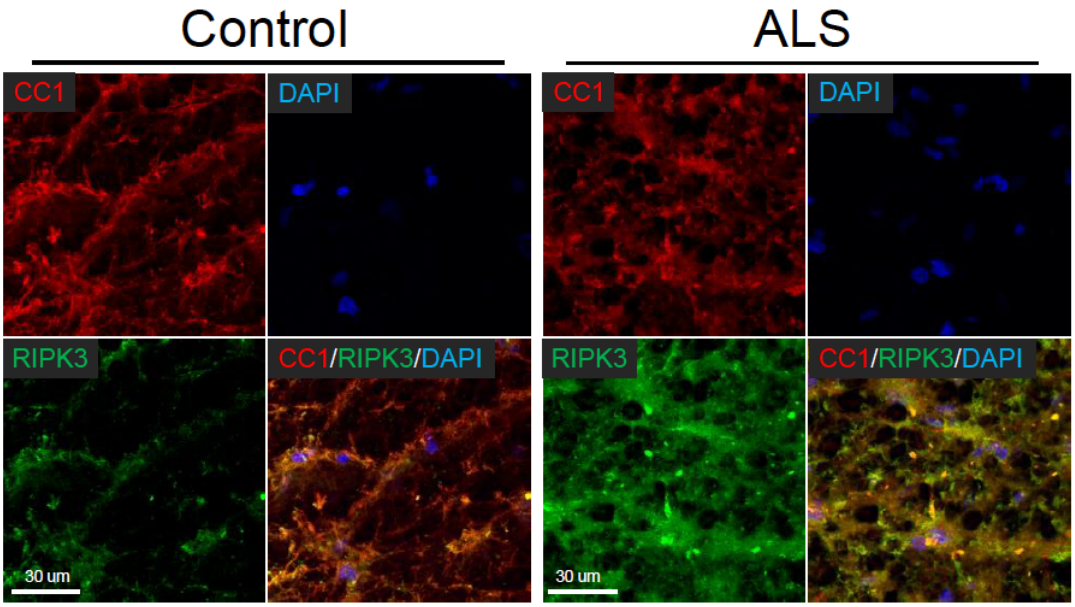
Control
ALS
CC1
DAPI
RIPK3
CC1/RIPK3/DAPI
30 um

C.

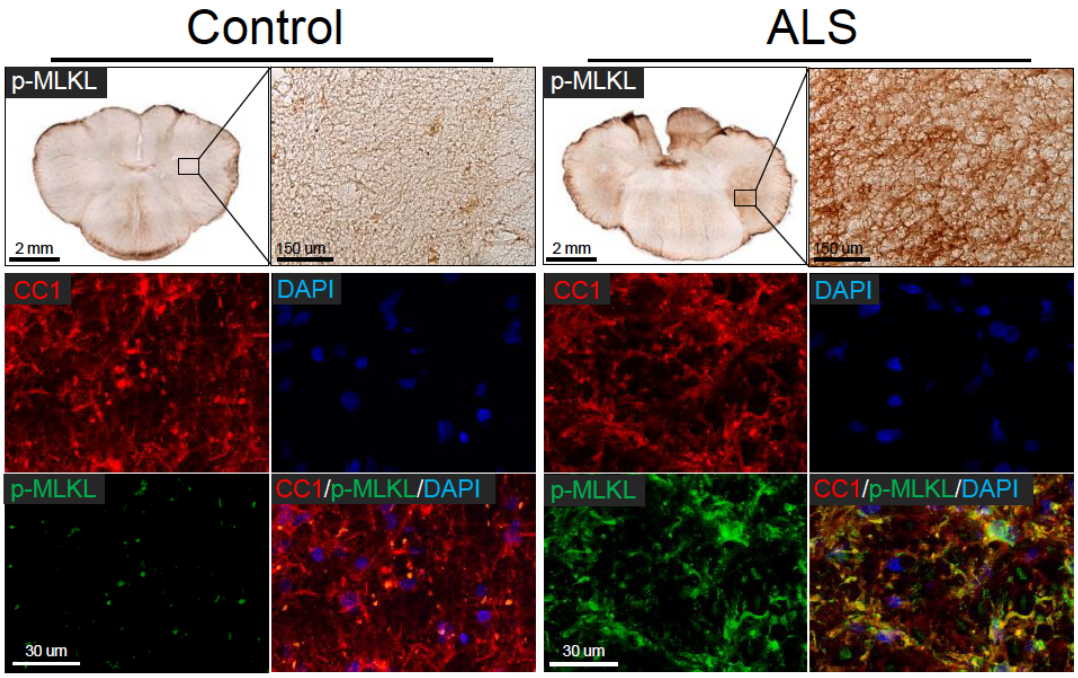
Control
ALS
p-MLKL
2 mm
150 um
CC1
DAPI
p-MLKL
CC1/p-MLKL/DAPI
30 um

Fig. S8

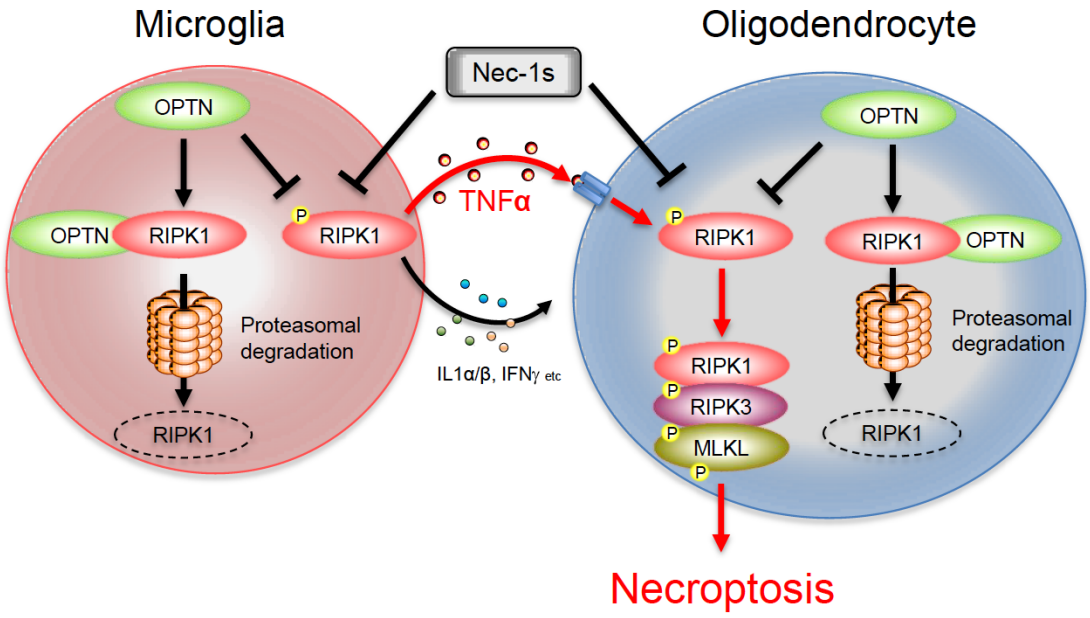
Microglia
Oligodendrocyte
Nec-1s
OPTN
OPTN
RIPK1
P
RIPK1
Proteasomal
degradation
RIPK1
TNFα
IL1α/β, IFNγ etc
OPTN
P
RIPK1
RIPK1
OPTN
Proteasomal
degradation
P
RIPK1
P
RIPK3
P
MLKL
P
RIPK1
Necroptosis

Table S1

Symbol	Name	Z-score
Ripk1	Receptor interacting serine/threonine kinase 1	6.89
Ripk3	Receptor-interacting serine-threonine kinase 3	2.60
Cyld	Cylindromatosis (turban tumor syndrome)	2.59
Optn	Optineurin	-2.07

Table S2

Symbol	Name	Location
Ctsb	Cathepsin B	8p23.1
Cd14	CD14 molecule (Myeloid Cell-Specific Leucine-Rich Glycoprotein)	5q31.3
Srxn1	Sulfiredoxin 1	20p13
Tcirg1	T-cell, immune regulator 1, ATPase, H+ transporting, lysosomal V0 subunit A3	11q13.2
Cnbp	CCHC-type zinc finger, nucleic acid binding protein	3q21
Ifrd1	Interferon-related developmental regulator 1	7q31.1
Chst11	Carbohydrate (chondroitin 4) sulfotransferase 11	12q23.3
Tes	Testin LIM domain protein	7q31.2
St6gal1	ST6 beta-galactosamide alpha-2,6-sialyltranferase 1	3q27.3
Gosr2	Golgi SNAP receptor complex member 2	17q21
Got1	Glutamic-oxaloacetic transaminase 1, soluble	10q24.1-q25.1
Got1	Golgi transport 1A	1q32.1
Got1	Golgi transport 1B	12p13.1
Gas7	Growth arrest-specific 7	17p13.1
Cerk	Ceramide kinase	22q13.31
Lrrfip1	Leucine rich repeat (in FLII) interacting protein 1	2q37.3
Cd86	CD86 molecule	3q21
Tgoln1	Trans-Golgi network protein	
Pi4k2a	Phosphatidylinositol 4-kinase type 2 alpha	10q24
Map4k4	Mitogen-activated protein kinase kinase kinase kinase 4	2q11.2-q12
Map4k3	Mitogen-activated protein kinase kinase kinase kinase 3	2p22.3
Il11ra1	Interleukin 11 Receptor, Alpha	9p13.3
Pde1b	Phosphodiesterase 1B, calmodulin-dependent	12q13
Hfe	Hemochromatosis	6p21.3
Cytip	Cytohesin 1 interacting protein	2q11.2
Pmaip1	Phorbol-12-myristate-13-acetate-induced protein 1	18q21.32
Arl5a	ADP-ribosylation factor-like 5A	2q23.3
Maff	v-maf avian musculoaponeurotic fibrosarcoma oncogene homolog F	22q13.1
Gpr34	G protein-coupled receptor 34	Xp11.4
Rel	v-rel avian reticuloendotheliosis viral oncogene homolog	2p13-p12
Cnn1	Calponin 1, basic, smooth muscle	19p13.2-p13.1

Table S3

Description	Gene Set Name	# Genes in Gene Set (K)	# Genes in Overlap (k)	k/K	p-value	FDR q-value
MAZ: MYC-associated zinc finger protein (purine-binding transcription factor)	GGGAGGRR_V$MAZ_Q6	2274	200	0.088	1.20E-53	1.01E-50
SP1: Sp1 transcription factor	GGGCGGR_V$SP1_Q6	2940	225	0.0765	2.86E-50	1.20E-47
LEF1: lymphoid enhancer-binding factor 1	CTTTGT_V$LEF1_Q2	1972	175	0.0887	3.21E-47	8.95E-45
NFAT: NFATC	TGGAAA_V$NFAT_Q4_01	1896	156	0.0823	5.22E-38	1.09E-35
TCF3: transcription factor 3 (E2A immunoglobulin enhancer binding factors E12/E47)	CAGGTG_V$E12_Q6	2485	176	0.0708	1.45E-34	2.42E-32
motif AACTTT: Motif does not match any known transcription factor	AACTTT_UNKNOWN	1890	147	0.0778	4.25E-33	5.92E-31
PAX4: paired box gene 4	GGGTGGRR_V$PAX4_03	1294	109	0.0842	2.02E-27	2.41E-25
ETS2: v-ets erythroblastosis virus E26 oncogene homolog 2 (avian)	RYTTCCTG_V$ETS2_B	1085	96	0.0885	8.35E-26	8.73E-24
ESRRA: estrogen-related receptor alpha	TGACCTY_V$ERR1_Q2	1043	92	0.0882	1.14E-24	1.06E-22
MLLT7: myeloid/lymphoid or mixed-lineage leukemia (trithorax homolog, Drosophila); translocated to, 7	TTGTTT_V$FOXO4_01	2061	137	0.0665	3.16E-24	2.64E-22

Table S4

No.	GUID #	Primary Diagnosis	Secondary Diagnosis	Age	Gender	Site of Onset	Disease Course (years)	PMI (hrs)
20	NA	Control	Basilar CVA	38	F	NA	NA	6
26	NA	Control	Cancer, obesity	49	M	NA	NA	4
31	NA	Control	Lung Cancer	67	M	NA	NA	3.5
39	NA	Control	Aortic Dissection & Multiple system failure	77	M	NA	NA	2
42	NA	Control	Brain Tumor	61	M	NA	NA	6
44	NA	Control	Liver failure	80	F	NA	NA	5
65	NA	Control		82	M	NA	NA	4
67	NA	Control		77	M	NA	NA	4
73	NA	Control	Cardiovascular and complications	74	M	NA	NA	5.5
78	NA	Control	Vasculitis, cerebral hemorrhage	58	F	NA	NA	3
30	NA	SALS	FTD vs PPA	73	M	Language & Respiratory	2.5	4.5
32	NA	SALS		71	M	Respiratory & trunk	1.5	4.5
33	NA	SALS		54	M	Arm	6.5	5
34	NA	SALS		81	F	Bulbar	1	3.5
35	NA	SALS		74	F	Bulbar	5.75	5
36	NA	SALS		73	M	Leg	1	5
38	NA	SALS v FALS	FTD w/ familal dementia 20 to MAPT (Arg5His) mutation	74	F	Dementia and Bulbar	2.75	4
43	NA	SALS		74	M	Respiratory and trunk	1.75	6
45	NA	SALS		69	F	Leg	5	5
47	NA	SALS		65	F	Bulbar	1.25	7
48	NA	SALS		67	M	Bulbar	1.75	6
60	NA	SALS		58	F	Bulbar	3	3
62	NA	SALS		52	M	Arm	1.5	6

References and Notes

1. E. Beeldman, A. J. van der Kooi, M. de Visser, M. C. van Maarle, F. van Ruissen, F. Baas, A Dutch family with autosomal recessively inherited lower motor neuron predominant motor neuron disease due to optineurin mutations. *Amyotroph. Lateral Scler. Frontotemporal Degener.* **16**, 410–411 (2015). Medline doi:10.3109/21678421.2015.1066821

2. E. T. Cirulli, B. N. Lasseigne, S. Petrovski, P. C. Sapp, P. A. Dion, C. S. Leblond, J. Couthouis, Y. F. Lu, Q. Wang, B. J. Krueger, Z. Ren, J. Keebler, Y. Han, S. E. Levy, B. E. Boone, J. R. Wimbish, L. L. Waite, A. L. Jones, J. P. Carulli, A. G. Day-Williams, J. F. Staropoli, W. W. Xin, A. Chesi, A. R. Raphael, D. McKenna-Yasek, J. Cady, J. M. Vianney de Jong, K. P. Kenna, B. N. Smith, S. Topp, J. Miller, A. Gkazi, A. Al-Chalabi, L. H. van den Berg, J. Veldink, V. Silani, N. Ticozzi, C. E. Shaw, R. H. Baloh, S. Appel, E. Simpson, C. Lagier-Tourenne, S. M. Pulst, S. Gibson, J. Q. Trojanowski, L. Elman, L. McCluskey, M. Grossman, N. A. Shneider, W. K. Chung, J. M. Ravits, J. D. Glass, K. B. Sims, V. M. Van Deerlin, T. Maniatis, S. D. Hayes, A. Ordureau, S. Swarup, J. Landers, F. Baas, A. S. Allen, R. S. Bedlack, J. W. Harper, A. D. Gitler, G. A. Rouleau, R. Brown, M. B. Harms, G. M. Cooper, T. Harris, R. M. Myers, D. B. Goldstein; FALS Sequencing Consortium, Exome sequencing in amyotrophic lateral sclerosis identifies risk genes and pathways. *Science* **347**, 1436–1441 (2015). Medline doi:10.1126/science.aaa3650

3. H. Maruyama, H. Morino, H. Ito, Y. Izumi, H. Kato, Y. Watanabe, Y. Kinoshita, M. Kamada, H. Nodera, H. Suzuki, O. Komure, S. Matsuura, K. Kobatake, N. Morimoto, K. Abe, N. Suzuki, M. Aoki, A. Kawata, T. Hirai, T. Kato, K. Ogasawara, A. Hirano, T. Takumi, H. Kusaka, K. Hagiwara, R. Kaji, H. Kawakami, Mutations of optineurin in amyotrophic lateral sclerosis. *Nature* **465**, 223–226 (2010). Medline doi:10.1038/nature08971

4. I. Munitic, M. L. Giardino Torchia, N. P. Meena, G. Zhu, C. C. Li, J. D. Ashwell, Optineurin insufficiency impairs IRF3 but not NF-κB activation in immune cells. *J. Immunol.* **191**, 6231–6240 (2013). Medline doi:10.4049/jimmunol.1301696

5. G. Zhu, C. J. Wu, Y. Zhao, J. D. Ashwell, Optineurin negatively regulates TNFalpha- induced NF-kappaB activation by competing with NEMO for ubiquitinated RIP. *Curr. Biol.* **17**, 1438–1443 (2007). Medline doi:10.1016/j.cub.2007.07.041

6. D. Ofengeim, J. Yuan, Regulation of RIP1 kinase signalling at the crossroads of inflammation and cell death. *Nat. Rev. Mol. Cell Biol.* **14**, 727–736 (2013). Medline doi:10.1038/nrm3683

7. S. He, L. Wang, L. Miao, T. Wang, F. Du, L. Zhao, X. Wang, Receptor interacting protein kinase-3 determines cellular necrotic response to TNF-alpha. *Cell* **137**, 1100–1111 (2009). Medline doi:10.1016/j.cell.2009.05.021

8. L. Sun, H. Wang, Z. Wang, S. He, S. Chen, D. Liao, L. Wang, J. Yan, W. Liu, X. Lei, X. Wang, Mixed lineage kinase domain-like protein mediates necrosis signaling downstream of RIP3 kinase. *Cell* **148**, 213–227 (2012). Medline doi:10.1016/j.cell.2011.11.031

9. D. W. Zhang, J. Shao, J. Lin, N. Zhang, B. J. Lu, S. C. Lin, M. Q. Dong, J. Han, RIP3, an energy metabolism regulator that switches TNF-induced cell death from apoptosis to necrosis. *Science* **325**, 332–336 (2009). Medline doi:10.1126/science.1172308

10. A. Degterev, J. Hitomi, M. Germscheid, I. L. Ch'en, O. Korkina, X. Teng, D. Abbott, G. D. Cuny, C. Yuan, G. Wagner, S. M. Hedrick, S. A. Gerber, A. Lugovskoy, J. Yuan, Identification of RIP1 kinase as a specific cellular target of necrostatins. *Nat. Chem. Biol.* **4**, 313–321 (2008). Medline doi:10.1038/nchembio.83

11. A. Degterev, Z. Huang, M. Boyce, Y. Li, P. Jagtap, N. Mizushima, G. D. Cuny, T. J. Mitchison, M. A. Moskowitz, J. Yuan, Chemical inhibitor of nonapoptotic cell death with therapeutic potential for ischemic brain injury. *Nat. Chem. Biol.* **1**, 112–119 (2005). Medline doi:10.1038/nchembio711

12. L. Conforti, J. Gilley, M. P. Coleman, Wallerian degeneration: An emerging axon death pathway linking injury and disease. *Nat. Rev. Neurosci.* **15**, 394–409 (2014). Medline doi:10.1038/nrn3680

13. M. C. Raff, A. V. Whitmore, J. T. Finn, Axonal self-destruction and neurodegeneration. *Science* **296**, 868–871 (2002). Medline doi:10.1126/science.1068613

14. J. T. Wang, Z. A. Medress, B. A. Barres, Axon degeneration: Molecular mechanisms of a self-destruction pathway. *J. Cell Biol.* **196**, 7–18 (2012). Medline doi:10.1083/jcb.201108111

15. S. Sasaki, S. Maruyama, Increase in diameter of the axonal initial segment is an early change in amyotrophic lateral sclerosis. *J. Neurol. Sci.* **110**, 114–120 (1992). Medline doi:10.1016/0022-510X(92)90017-F

16. L. Zhuo, M. Theis, I. Alvarez-Maya, M. Brenner, K. Willecke, A. Messing, hGFAP-cre transgenic mice for manipulation of glial and neuronal function in vivo. *Genesis* **31**, 85–94 (2001). Medline doi:10.1002/gene.10008

17. B. E. Clausen, C. Burkhardt, W. Reith, R. Renkawitz, I. Förster, Conditional gene targeting in macrophages and granulocytes using LysMcre mice. *Transgenic Res.* **8**, 265–277 (1999). Medline doi:10.1023/A:1008942828960

18. C. Lappe-Siefke, S. Goebbels, M. Gravel, E. Nicksch, J. Lee, P. E. Braun, I. R. Griffiths, K. A. Nave, Disruption of Cnp1 uncouples oligodendroglial functions in axonal support and myelination. *Nat. Genet.* **33**, 366–374 (2003). Medline doi:10.1038/ng1095

19. C. N. Parkhurst, G. Yang, I. Ninan, J. N. Savas, J. R. Yates 3rd, J. J. Lafaille, B. L. Hempstead, D. R. Littman, W. B. Gan, Microglia promote learning-dependent synapse formation through brain-derived neurotrophic factor. *Cell* **155**, 1596–1609 (2013). Medline doi:10.1016/j.cell.2013.11.030

20. D. E. Christofferson, J. Yuan, Necroptosis as an alternative form of programmed cell death. *Curr. Opin. Cell Biol.* **22**, 263–268 (2010). Medline doi:10.1016/j.ceb.2009.12.003

21. J. Hitomi, D. E. Christofferson, A. Ng, J. Yao, A. Degterev, R. J. Xavier, J. Yuan, Identification of a molecular signaling network that regulates a cellular necrotic cell death pathway. *Cell* **135**, 1311–1323 (2008). Medline doi:10.1016/j.cell.2008.10.044

22. D. E. Christofferson, Y. Li, J. Hitomi, W. Zhou, C. Upperman, H. Zhu, S. A. Gerber, S. Gygi, J. Yuan, A novel role for RIP1 kinase in mediating TNFα production. *Cell Death Dis.* **3**, e320 (2012). Medline doi:10.1038/cddis.2012.64

23. A. Polykratis, N. Hermance, M. Zelic, J. Roderick, C. Kim, T. M. Van, T. H. Lee, F. K. Chan, M. Pasparakis, M. A. Kelliher, Cutting edge: RIPK1 kinase inactive mice are viable and protected from TNF-induced necroptosis in vivo. *J. Immunol.* **193**, 1539–1543 (2014). Medline doi:10.4049/jimmunol.1400590

24. D. Ofengeim, Y. Ito, A. Najafov, Y. Zhang, B. Shan, J. P. DeWitt, J. Ye, X. Zhang, A. Chang, H. Vakifahmetoglu-Norberg, J. Geng, B. Py, W. Zhou, P. Amin, J. Berlink Lima, C. Qi, Q. Yu, B. Trapp, J. Yuan, Activation of necroptosis in multiple sclerosis. *Cell Rep.* **10**, 1836–1849 (2015). Medline doi:10.1016/j.celrep.2015.02.051

25. P. Langfelder, S. Horvath, WGCNA: An R package for weighted correlation network analysis. *BMC Bioinformatics* **9**, 559 (2008). Medline doi:10.1186/1471-2105-9-559

26. K. A. Kigerl, J. C. Gensel, D. P. Ankeny, J. K. Alexander, D. J. Donnelly, P. G. Popovich, Identification of two distinct macrophage subsets with divergent effects causing either neurotoxicity or regeneration in the injured mouse spinal cord. *J. Neurosci.* **29**, 13435–13444 (2009). Medline doi:10.1523/JNEUROSCI.3257-09.2009

27. A. Subramanian, P. Tamayo, V. K. Mootha, S. Mukherjee, B. L. Ebert, M. A. Gillette, A. Paulovich, S. L. Pomeroy, T. R. Golub, E. S. Lander, J. P. Mesirov, Gene set enrichment analysis: A knowledge-based approach for interpreting genome-wide expression profiles. *Proc. Natl. Acad. Sci. U.S.A.* **102**, 15545–15550 (2005). Medline doi:10.1073/pnas.0506580102

28. S. I. Berger, J. M. Posner, A. Ma'ayan, Genes2Networks: Connecting lists of gene symbols using mammalian protein interactions databases. *BMC Bioinformatics* **8**, 372 (2007). Medline doi:10.1186/1471-2105-8-372

29. S. H. Kang, Y. Li, M. Fukaya, I. Lorenzini, D. W. Cleveland, L. W. Ostrow, J. D. Rothstein, D. E. Bergles, Degeneration and impaired regeneration of gray matter oligodendrocytes in amyotrophic lateral sclerosis. *Nat. Neurosci.* **16**, 571–579 (2013). Medline doi:10.1038/nn.3357

30. D. B. Re, V. Le Verche, C. Yu, M. W. Amoroso, K. A. Politi, S. Phani, B. Ikiz, L. Hoffmann, M. Koolen, T. Nagata, D. Papadimitriou, P. Nagy, H. Mitsumoto, S. Kariya, H. Wichterle, C. E. Henderson, S. Przedborski, Necroptosis drives motor neuron death in models of both sporadic and familial ALS. *Neuron* **81**, 1001–1008 (2014). Medline doi:10.1016/j.neuron.2014.01.011

31. T. W. Gould, R. R. Buss, S. Vinsant, D. Prevette, W. Sun, C. M. Knudson, C. E. Milligan, R. W. Oppenheim, Complete dissociation of motor neuron death from motor dysfunction by Bax deletion in a mouse model of ALS. *J. Neurosci.* **26**, 8774–8786 (2006). Medline doi:10.1523/JNEUROSCI.2315-06.2006

32. J. J. Peschon, D. S. Torrance, K. L. Stocking, M. B. Glaccum, C. Otten, C. R. Willis, K. Charrier, P. J. Morrissey, C. B. Ware, K. M. Mohler, TNF receptor-deficient mice reveal divergent roles for p55 and p75 in several models of inflammation. *J. Immunol.* **160**, 943–952 (1998). Medline

33. T. Osawa, Y. Mizuno, Y. Fujita, M. Takatama, Y. Nakazato, K. Okamoto, Optineurin in neurodegenerative diseases. *Neuropathology* **31**, 569–574 (2011). Medline doi:10.1111/j.1440-1789.2011.01199.x

34. H.-X. Deng, E. H. Bigio, H. Zhai, F. Fecto, K. Ajroud, Y. Shi, J. Yan, M. Mishra, S. Ajroud-Driss, S. Heller, R. Sufit, N. Siddique, E. Mugnaini, T. Siddique, Differential involvement of optineurin in amyotrophic lateral sclerosis with or without *SOD1* mutations. *Arch. Neurol.* **68**, 1057–1061 (2011). Medline doi:10.1001/archneurol.2011.178

35. K. Newton, X. Sun, V. M. Dixit, Kinase RIP3 is dispensable for normal NF-kappa Bs, signaling by the B-cell and T-cell receptors, tumor necrosis factor receptor 1, and Toll-like receptors 2 and 4. *Mol. Cell. Biol.* **24**, 1464–1469 (2004). Medline doi:10.1128/MCB.24.4.1464-1469.2004

36. Y. Chen, V. Balasubramaniyan, J. Peng, E. C. Hurlock, M. Tallquist, J. Li, Q. R. Lu, Isolation and culture of rat and mouse oligodendrocyte precursor cells. *Nat. Protoc.* **2**, 1044–1051 (2007). Medline doi:10.1038/nprot.2007.149

37. J. Saura, J. M. Tusell, J. Serratosa, High-yield isolation of murine microglia by mild trypsinization. *Glia* **44**, 183–189 (2003). Medline doi:10.1002/glia.10274

38. L. Mayo, S. A. Trauger, M. Blain, M. Nadeau, B. Patel, J. I. Alvarez, I. D. Mascanfroni, A. Yeste, P. Kivisäkk, K. Kallas, B. Ellezam, R. Bakshi, A. Prat, J. P. Antel, H. L. Weiner, F. J. Quintana, Regulation of astrocyte activation by glycolipids drives chronic CNS inflammation. *Nat. Med.* **20**, 1147–1156 (2014). Medline doi:10.1038/nm.3681

39. H. Wang, L. Sun, L. Su, J. Rizo, L. Liu, L. F. Wang, F. S. Wang, X. Wang, Mixed lineage kinase domain-like protein MLKL causes necrotic membrane disruption upon phosphorylation by RIP3. *Mol. Cell* **54**, 133–146 (2014). Medline doi:10.1016/j.molcel.2014.03.003

40. X. Xie, J. Lu, E. J. Kulbokas, T. R. Golub, V. Mootha, K. Lindblad-Toh, E. S. Lander, M. Kellis, Systematic discovery of regulatory motifs in human promoters and 3′ UTRs by comparison of several mammals. *Nature* **434**, 338–345 (2005). Medline doi:10.1038/nature03441